Microstructure observations of the summer-to-winter destratification at a coastal site in the Gulf of Naples.

Florian Kokoszka[1], Fabio Conversano[1], Daniele Iudicone[1], Bruno Ferron[2], Pascale Bouruet-Aubertot[3], Justine Mc Millan[4]

[1]Stazione Zoologica Anton Dohrn, Naples, Italy
[2]Univ. Brest, CNRS, IFREMER, IRD, Laboratoire d'Océanographie Physique et Spatiale (LOPS),
IUEM, Plouzané, France
[3]Sorbonne Université (UPMC, Univ Paris 06)-CNRS-IRD-MNHN, LOCEAN, Paris, France
[4]Rockland Scientific International Inc., Victoria, Canada

Key Points:

- A good agreement is obtained in the mixed layer depth (MLD) between ϵ_{VMP} and the model of Belcher et al. [2012] that combines the contribution of wind, wave (Langmuir cells), and buoyancy forcings.
- The model is estimated from bulk parameters (ERA5 data set), and used to identify the sequence of processes and their relative contribution to dissipation.
- Comparisons are closer to observations when estimating dissipation from the model nearly ~ 10 hours before the cast, that confirm the time scale for the adjustment of the stratification to the forcings observed by Lozovatsky et al. [2005].
- Significant correlations are found between wind stress and ϵ in the internal layer during the previous 24 hours and 4.25 days, suggesting that internal waves generated by the wind can setup the mixing intensity despite the lack of tidal forcing.
- This suggest that in the shallow coastal area the stratification is seasonally eroded at the water-column boundaries, associated respectively to wind, wave, and buoyancy forcings in subsurface, and internal waves motions in the internal layers.

Corresponding author: Florian Kokoszka, `florian.kokoszka@szn.it`

Abstract

A dissection of the physics of seasonal cycle of oceanic upper layer stratification is necessary to improve climate predictions of biogeochemical cycles. We present a time series of vertical profiles of ϵ, the dissipation rate of turbulent kinetic energy, obtained from a microstructure profiler during the destratification period (summer-to-winter) at a mid-latitude 75m-deep coastal site. Significant correlation is obtained in the mixed layer depth (MLD) with a model combining effects of wind, wave, and buoyancy forcings, estimated from bulk parameters ~ 10 hours before observations, and used to identify the dominant forcings leading to MLD deepening. Intermittency at surface is correlated with seasonal storminess, and we observe a quadratic relation between kurtosis and skewness for ϵ statistics. By splitting the time series into layers, we observe the co-location of patches of higher ϵ with the shear maxima of the two first baroclinic modes, and significant correlations with surface wind stress in the transitional layer the past 24 hours, and at longer scale (4.25 days) in the baroclinic layer, suggesting that internal waves activity influences the setup of mixing intensity despite the lack of tidal forcing. The low-passed microstructure shear distribution seems to support this hypothesis despite possible signal contamination. In the highly stratified layers associated to salt-fingering (MLD's basis and below), the buoyancy Reynolds number indicates a buoyancy regime control with low mixing value (0.2×10^{-5} m^2 s^{-1}). More turbulent flows are identified in both surface and bottom layers (0.6 to 0.8×10^{-5} m^2 s^{-1}), suggesting a seasonal erosion of the stratification by the boundary processes.

Plain Language Summary

Numerical models predict an increase of the vertical gradient of density between ocean surface and deep layers, linked to climate change and impacting currents and vertical supply of nutrients. We present a time survey describing mixing in the ocean, the water properties redistribution of the water-column, during summer to winter at a Mediterranean Sea coastal site. Significant correlation is obtained between measurements of energy dissipation in the surface homogeneous layer and an estimation modeling effects of wind, wave, and convection due to atmospheric cooling during the previous night. We interpret their influence on the surface homogeneous layer thickness which deepens progressively from end of summer to reach the bottom in winter. Measurements reproduce the intermittency and amplitude of such transitory events. In the stable part of the water-column, energy is distributed vertically where internal oscillations are expected. Correlations are found between energy loss in stable layer and the surface wind friction in the past 24 hours and at 4.25 days, suggesting that internal motions due to wind influence mixing. Turbulent activity parameters indicate quiescent flow in the internal intermediary layers associated to downwards transfer of salt and a weak capacity to mix. More turbulent flows are identified in both surface and bottom, suggesting a seasonal erosion of the stability of the water-column at its boundaries.

1 Introduction

The stratification of the oceans, that is, the density change with depth, regulates the physical processes taking place from the surface to the bottom (Garrett et al. [1978], de Boyer Montégut et al. [2004]). Its vertical structure, related to the vertical structure of temperature and salinity, results from the transfer of energy of large-scales forcings (e.g., winds, sea-air and ice-air buoyancy exchanges, tides) toward small dissipative scales (Wunsch & Ferrari [2004], S. A. Thorpe [2005]). The transfer of energy occurs via a large variety of phenomena (e.g., internal waves, eddies, filaments, overturns Ferrari & Wunsch [2009]), whose roles are not perfectly disentangled. In addition, forcing sources may be remote. These different processes are regulated by the stratification which, in turn, is modified through the micro-scale mixing they ultimately provide (Brainerd & Gregg [1995], Mackinnon & Gregg [2005]). As discussed in Somavilla et al. [2017], the link between surface forcing and stratification is made more complex by the preconditioning role that surface forcing have on the permanent pycnocline. In a context of data analyses and projections that indicate that global warming leads to stronger stratification (Skliris et al. [2014], Hegerl et al. [2015], Zika et al. [2015], Pastor et al. [2018], Guancheng et al. [2020]), it is of importance to identify which processes that regulate the stratification are the most sensitive to changes.

More generally, the relative importance of specific physical processes acting on the vertical distribution of temperature and salinity strongly varies during the year, leading to an important seasonality of the interplay of fine-scale processes over the vertical dimension (Brody et al. [2014]). The seasonal conditioning of the water column stratification regulates also the biological activity since it controls the vertical transfer and uptakes of nutrients (Sverdrup [1953], Kiørboe & Mackenzie [1995]), while several marine species take advantage or are limited by the water motions modulated by the stratification (Mann & Lazier [1996], Prairie et al. [2012], Barton et al. [2014], Wheeler et al. [2019]). Understanding its seasonality in relation to mixing is thus relevant for the biogeochemicals cycles, harmful algae blooms and plastic dispersal, among others (Sverdrup [1953], Pingree et al. [1976], Wihsgotta et al. [2019]). Mixing observations through dedicated high resolution profilers have multiplied since the first designs of microstructure probes in the 1960's (Osborn [1998], Lueck et al. [2002], Shang et al. [2016]) to better understand how energy transfers toward small scales (in the ocean). But the difficulty of the deployment at sea and the complexity of the physical phenomena to be sampled make an in situ characterization challenging. Thus, an effort toward the acquisition of high quality data at all scales, from the open ocean to the coastal area, remains a primer. Additionally, once acquired the data interpretation remains difficult since it is not always possible to disentangle the role of single processes as pointed also by the recent study of Lozovatsky et al. [2017]. For this task, studies based on detailed continuous observations are a primer, as the recent works of Haren [2019] and Haren et al. [2020] in lakes, that describe the impact of the seasonal interplay between wind stress, internal waves and convection to the mixing in such specific locations.

Coastal marine ecosystem such as the Gulf of Naples is a mid-latitude semi-enclosed shallow basin in the Western Mediterrean Sea having a subtropical regime and almost no tides (**Fig. 1**). The area presents a marked salinity contrast due to the combination of the salty Tyrrhenian Sea waters, with its own feature of inshore/offshore water exchange with the open ocean, located on its southern side (Cianelli et al. [2015]), and the freshwater inputs from a densely inhabited coastal area, on its northern part and from nearby rivers (Cianelli et al. [2012], Cianelli et al. [2017]). Forced also by recurrent, highly seasonal intense wind forcing events, its cross-shore exchanges are modulated by mesoscale eddies and sub-mesoscale filaments (Iermano et al. [2012]). The important role of lateral transport of freshwater in setting the stratification by straining the water-column (Verspecht et al. [2009]) implies also that long term changes are possibly impacted also by the effects of climate change on the surrounding territories, which include regions with

important winter snow accumulations. Thus, the study area is an ideal site to study how coastal salinity and temperature changes combine in setting the variability of the vertical stratification (Woodson [2018]), in a context of rising air and sea temperatures and of intensifying extreme events such as storms, floods and even, recently, Mediterranean hurricanes (Volosciuk et al. [2016], Koseki et al. [2020], W. Zhang et al. [2020]). In terms of mechanical forcing, coastal areas have been showed to respond specifically to the wind forcing, such as the local the wind flow aligning with the main circulation in function of the terrestrial relief and geometry of the coastline, possibly enhancing significantly the turbulent events (Burchard & Rippeth [2009]). More generally, boundary effects at the bottom due to the shallow depth are expected, such as sediment re-suspension, related to direct drag effects, or even due to the generation of internal waves (Haren et al. [2019]). As pointed in the study of Lucas et al. [2019], interaction between the wind and the wave field, through the regime of Langmuir circulation cells, should be important in such shallow and enclosed areas, and contribute significantly to mix the stratification, by enhancing the shear-driven turbulence (S. Li et al. [2013]), and/or adding its effect to the convective destabilizing events (Q. Li & Fox-Kemper [2017]). All of these points depict the complexity of the interplay between processes in coastal areas, and their impact on the observed stratification. Variations in the seasonality of heat fluxes and redistribution of freshwater inputs due to climate change still have to be determined, in the same way than the variability of the mechanical forcing of the wind, and its interactions with the wave field. Contribution of mesoscale through water parcels mixing and advection remains to be investigated too, taking in account the coupling between sub-mesoscale filaments and Langmuir cells that could strongly influence the circulation in the surface layers (Sullivan & McWilliams [2019]). Ultimately, times series of observations of mixing (main values, location, and intermittency) are of importance for improving the predictions of numerical simulations (Pearson & Fox-Kemper [2018], Benway et al. [2019]).

Our study provides a direct observation of turbulent mixing associated to the seasonal de-strafication period, in a coastal shallow-water area with almost no tides, and a first identification of the processes that should be investigated to improve the understanding of the dynamics of such area, and the predictions of the marine ecosystems evolution. We present a unique attempt to describe the seasonal cycle of the vertical stratification and associated mixing with high-resolution data collected from July 2015 to February 2016. These observations contribute to the Long Term Ecosystem Research Marechiara (LTER-MC) initiative that produced a historical time series of a Mediterranean coastal ecosystem through a weekly sampling of the water column started in 1984 and running until now (Ribera d'Alcala et al. [2004], Zingone et al. [2019]). We propose to identify the processes accompanying the seasonal de-stratification of the water-column, during the course of the mixed layer depth deepening weeks after weeks, through the analysis of the time series of the mixed and stratified layers, and the temporal sequence of the surface forcing.

2 Materials and Methods

Overview of the study

First, we propose to compare the time evolution of the mixed layer depth in function of the seasonal context of the forcings of wind stress and buoyancy fluxes. For this, we will analyze their interplay through the Monin-Obhukov length scale (Obukhov [n.d.], Obukhov [1971]) and try to identify periods of their respective dominances, to guide then the analysis of observations of turbulence made with a micro-structure profiler. Making the hypothesis that the observed dissipation rates of turbulent kinetic energy result from a combination of processes that transfer their energy toward dissipative scales, we attempt to disentangle between the respective role of convection, wind and waves in the surface layers, by comparing in-situ micro-structure measurements to the model of Belcher et al. [2012], that use bulk parameters associated to these forcings through the Langmuir number and the Monin-Obhukov length scales, and could be useful to interpret the temporal evolution of the dominant processes. Internal layers susceptible to intermittent diffusive convection and double diffusion regimes will be investigated too as they may be impacted by changes in the vertical stability. Below the mixed layer depth, surface forcings such as wind are susceptible to generate internal waves at the transitional depth between mixed and stratified layers, and we present the distributions of dissipation rates and mixing observed in the layers containing the main part of energy of the two first baroclinic modes, to characterize the expected intermittency in such parts of the water-column, to compare it to surface, and contribute to propose benchmark dataset that could help to validate models and numerical simulations. By correlating the time series of epsilon in these layers to the surface wind stress and buoyancy fluxes, we propose to infer the time scale at which the wind events can sustain internal waves activity into the water-column, as observed in the Gulf of Naples. This coastal system being shallow, a strong influence of the bottom acting as a boundary layer is expected, and a statistic of epsilon in the bottom layer will be provided too, to complete the overview of distribution of epsilon in function of the layers and the mean value of stratification. We will conclude then by depicting a conceptual scheme that illustrates the process overview during the summer-to-winter transition.

2.1 Hydrology and mixed layer depth (MLD)

Conductivity–Temperature–Depth (CTD) profiles were carried out at the LTER-MC sampling point in the Gulf of Naples (**Fig. 1**) with a Seabird `SBE-911+` mounted on a 12-bottle carousel, with all sensors calibrated. The raw $24\,$Hz profiles were processed using the Seabird data processing SeaSave 7.26.7 to obtain 1-m bin-averaged data. The weekly survey refers to the casts MC1160 to MC1190 and includes a total of 31 CTD profiles (supplementary Tab. S1). Independent to these data, the vertical microstructure profiler (`VMP-250` from Rockland Scientific International Inc, henceforth reffered to as Rockland) used in this study was equipped with a nose-mounted high-precision conductivity-temperature sensors (micro-CT) from JFE Advantech, sampling at $64\,$Hz. These data were averaged on a regular vertical grid of 10 cm, and allowed us to collect a second hydrological dataset, directly co-located with the microstructure measurements. CTD data were used to provide a general view on the hydrological context of our study (periods of external forcings, mixed layer depth, vertical internal layers of the water-column), and micro-CT data to infer the Turner's regimes (see Section 2.2). For both datasets, the Gibbs-SeaWater Oceanographic Toolbox (McDougall & Barker [2011]) was used to calculate the conservative temperature Θ (°C), the absolute salinity A_S (g kg^{-1}), the water density anomaly ρ (kg m^{-3}), the potential density σ_0 (kg m^{-3}), the potential temperature θ_0 (°C), and the Brunt-Väisälä frequency N^2 (s^{-2}). When mentioned thereafter, T and S refer to Θ and A_S. Mixed layer depth (MLD, m) was calculated following the method of de Boyer Montégut et al. [2004] based on threshold values. Given a vertical profile of density $\sigma_0(z)$, or potential temperature $\theta_0(z)$, we calculated the depth below $z_{ref} = 3\ m$,

210   where the profile reached thresholds defined as a cumulative of $0.4°C$ for θ_0, and $0.03\ kg\ m^{-3}$
211   for σ_0. The VMP was also equipped with a fluorometer-turbidity sensor from JFE Ad-
212   vantech, sampling at $512\,\text{Hz}$. These data were converted to physical units using the ODAS
213   Matlab Toolbox provided by Rockland (version 4.4.06). The sensor has a spatial response
214   of $\sim 1\,\text{cm}$ (Wolk et al. [2002]) and the data were averaged over $10\,\text{cm}$. A mean value of
215   $-2.5\,\text{FTU}$ (Formazin Turbidity Units) over the whole cast was taken as a reference to
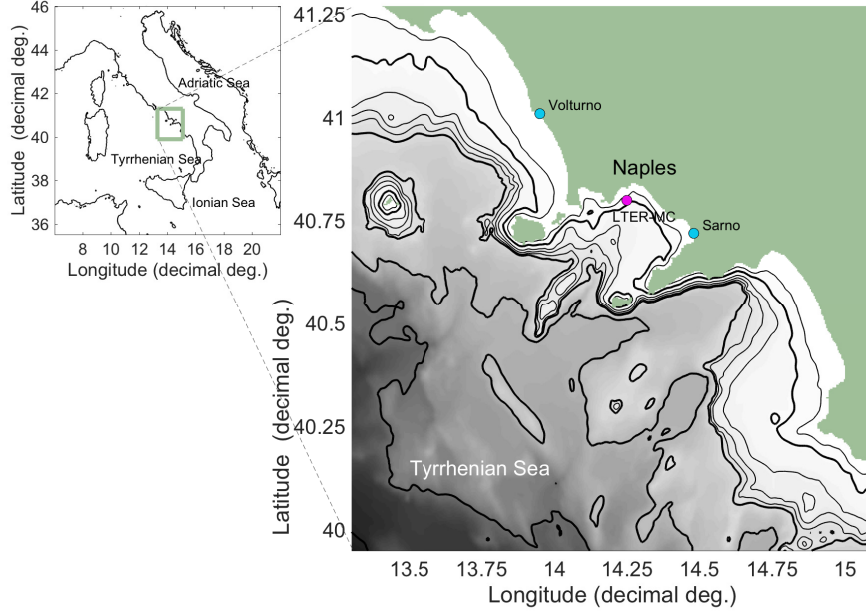216   establish a ΔFTU and identify turbid layers in the water-column.

Figure 1: Bathymetry of the Gulf of Naples (GEBCO grid [GEBCO, 2020]) along the Tyrrhenian Sea in the Mediterranean basin). The 75m-deep LTER-MC coastal sampling site ($14.25°E, 40.80°N$) is located by the pink dot. Volturno and Sarno's river mouths are shown in blue. Thin lines indicate the 50, 200, 300 and 400 m isobaths, thick ones indicate the 100, 500, 1000 and 2000 m isobaths.

2.2   Turner's regimes

218   We applied the method introduced by Turner (Turner [1967], [1973]) to localize parts
219   of the water column where vertical gradients of T and S are favourable to double-diffusive
220   instability. The high-resolution CT data from the JFE Advantech sensor mounted on
221   the `VMP-250` was used for this analysis. Combining the vertical gradients and their signs
222   allows the identification of stability regimes, that can be defined from the ratio $R_\rho =$
223   $(\alpha d\theta/dz)/(\beta dS/dz)$ where $\alpha = -\rho^{-1}(d\rho/d\theta)$ is the thermal expansion coefficient, $\beta =$
224   $\rho^{-1}(d\rho/dS)$ is the haline contraction coefficient, where $d\rho/dz$ and $d\theta/dz$ are the verti-
225   cal gradients of density and temperature, respectively. This ratio is used to calculate the
226   Turner angles (°) $Tu = \arctan((1 + R_\rho)/(1 - R_\rho))$ (Ruddick [1983]). The value of the
227   Turner angle defines various stability regimes. A diffusive convection regime (e.g., fresh
228   cold layers over warm salty layer) arises when $-90° < Tu < -45°$. A double-diffusive
229   regime (e.g., salty warm layer over cold fresh layer) arises when $45° < Tu < 90°$. Within
230   each of these regimes, the instability is higher when $|Tu|$ is close to 90 degrees. A sta-
231   ble regime occurs when $|Tu| < 45°$, whereas a gravitationally unstable regime occurs
232   when $|Tu| > 90°$.

2.3 Bulk parameters of atmospheric forcings

Surface heat fluxes (latent and sensible, with net solar and thermal radiation), wind velocities (U_{10} and V_{10}), evaporation E and precipitation rates P, period and significant height H_S of waves were extracted from the ERA5 re-analysed product provided by Copernicus (ERA5(C3S) [2017]). The closest grid-point was selected from the LTER-MC geographical position ($14.25°E$ and $40.80°N$), with a 6-hour temporal resolution, over the whole period. These bulk parameters are used to infer the Monin-Obukhov length scale L_{MO} (Obukhov [n.d.], Obukhov [1971]), a critical length scale describing the depth at which the turbulence is dominated by wind shear more than buoyancy forcings. The Monin-Obukhov length scale is defined as $L_{MO} = u_*^3/\kappa B$ (m). Here u_* is the friction velocity of the wind ($\mathrm{m\,s^{-1}}$), κ the von Karman's constant (here 0.4), and B the buoyancy flux ($\mathrm{m^2\,s^{-3}}$), defined such that $B > 0$ if stabilizing the water-column. Buoyancy flux is proportional to the density flux at the surface, as $B = gQ_p/\rho_0$, where the density flux Q_p into the ocean from the atmosphere was computed as (H.-M. Zhang & Talley [1998]) $Q_p = \rho(\alpha F_T + \beta F_S)$, with α and β the thermal expansion and saline contraction coefficients, respectively. Here $F_T = -Q_{net}/\rho_{sea}C_p$, and $F_S = (E - P)S/(1 - S/1000)$, where C_p is the specific heat of seawater, E, P, and S are the evaporation, precipitation and sea surface salinity. The net radiative heat flux at the ocean surface Q_{net} ($\mathrm{W\,m^{-2}}$) was calculated from the combination of the incoming short wave, net incoming and emitted long wave, sensible and latent heat. The velocity friction u_* was calculated as $u_* = \sqrt{\tau/\rho_{sea}}$, where ρ_{sea} is the density of seawater, and τ the wind stress, as $\tau = \rho_{air}C_D U_{10}^2$, where $\rho_{air} = 1.22\ \mathrm{kg\,m^{-3}}$, and drag coefficient C_D and velocity at $10\,\mathrm{m}$ U_{10} calculated from wind velocity following Large & Pond [1981]. Wind stress dominance over stable B can be identified from the L_{MO} diagnostic ($L_{MO} > 1$), and the other different regimes are shown after on **Fig. 3.c**. To extend the analysis to the effect of waves, we calculated the Langmuir number La (Leibovich [1983]) that relies on the interaction between the Stokes drift and the wind-forced surface shear. Under favourable conditions between wind and sea-state, the wave field can generate vertically aligned Langmuir circulations cells (S. Thorpe [2004]) that can contribute significantly to the mixing in the surface layers. The Langmuir number is defined as $La = \sqrt{u_*/u_s}$, where u_s is the Stokes drift velocity, and considered to be critical for wave dominance when its values are close to 0.5 and below (Belcher et al. [2012]). To estimate this quantity from bulk parameters including the local surface wind effect, we apply the parameterization of Ardhuin et al. [2009], (discussed thoroughly in Sayol et al. [2016]) : $u_s = 5\times10^{-4}(1.25 - 0.25(0.5/f_c)^{1/3})W_{10}W_{10}^m + 0.025(H_s - 0.4)$, where $f_c = 0.5\ \mathrm{Hz}$ refers to the cut-off frequency, W_{10}^m an upper threshold for wind module ($W_{10}^m = W_{10}$ if $W_{10} < 14.5\mathrm{m\,s^{-1}}$, or $= 14.5$ if $W_{10} > 14.5\mathrm{m\,s^{-1}}$), and H_s the significant wave height, whose values $< 0.4\mathrm{m}$ were not considered into the estimation. For these values, u_s was considered $= 0$ and $La = \infty$.

2.4 Turbulent kinetic energy dissipation rate estimates from bulk parameters

Taking into account the direct contribution of buoyancy and mechanical mixing at the air-sea interface to the evolution of the ocean surface boundary layer, Belcher et al. [2012] derived a parameterization (mentioned thereafter as B12) for ϵ as the result of a linear combination of wind stress, wave-wind interaction through the Langmuir circulation cells, and buoyancy forcing due to destabilising convection, valid at the depth where the three forms of turbulence are considered to be well established. This formulation derives from an universal function using the mixing or mixed layer length scale h, the wind friction u_*^3, the Langmuir number La, the convection velocity scale $w_* = (Bh)^{1/3}$ (only for destabilising buoyancy fluxes, here with $B < 0$), and the velocity scale for wave-forced turbulence $w_{*L} = (u_*^2 u_s)^{1/3}$. Dissipation rate of turbulent kinetic energy is given by the linear combination of the effect of wind, wave, and convection at the depth $h/2$, as $\epsilon_{B12} = E_S u_*^3/h + E_L w_{*L}^3/h + E_C w_*^3/h$, with $E_S = 2(1 - e^{-La/2})$, $E_L =$

0.22 (Grant & Belcher [2009]), $E_C = 0.3$ (Moeng & Sullivan [1994]). This equation leads to the Langmuir stability length $L_L = w_{*L}^3/B$ as a scaling argument, which is analogue for convective-Langmuir of the Monin-Obhukov length L_{MO} for convective-shear turbulence (S. A. Thorpe [2005]) : when $h/L_L < 1$ wave forcing dominates the mixing in the surface layer, and when $h/L_L > 1$ buoyancy forcing dominates. Note that L_L is estimated only when B is destabilising, i.e., cooling the ocean (here $B < 0$), in the contrary of the Monin-Obhukov that is generally used to infer wind dominance against stabilizing fluxe (here $B > 0$).

Comparisons between model and observations are evaluated at $h/2$, with $h = \text{MLD}$. Sutherland et al. [2014] found a better agreement when taking into account the mixing layer depth instead of the MLD. This vertical length is defined as the depth at which ϵ falls to a background level of $1 \times 10^{-9}\,\text{W}\,\text{kg}^{-1}$, but the vertical variability of our observations of ϵ (see the next subsection about micro-structure data, and the dedicated section of results) did not allow us to determine it with the same definition, and the MLD was considered as the scaling for h.

2.5 Microstructure data

Microstructure measurements were collected at the LTER-MC point using a `VMP-250` profiler from Rockland. During each deployment, between one and four profiles were completed down to five meters above the bottom (75 m deep), resulting in a total of 71 profiles among the 31 weekly CTD profiles of the survey (supplementary Tab. S1). The profiler was deployed with a tether from the ship and fell quasi-freely at a speed of $0.7\,\text{m}\,\text{s}^{-1}$ to $0.9\,\text{m}\,\text{s}^{-1}$. The profiler was equipped with two microstructure shear sensors, a fast response temperature sensor (FP07) and a micro-conductivity sensor (SBE7), which were all sampled at $512\,\text{Hz}$. The shear probes measured the vertical shear of horizontal velocity fluctuations (i.e. du/dz, dv/dz). The raw signals are subject to noise and signal contamination from instrument vibrations, internal circuitry, and impact of biology and sediment. To reduce the impact of signal contamination, several processing steps were required before computing the spectra and dissipation rate. Firstly, the upper and lower meters of each cast, where the profiler was accelerating and decelerating, were discarded. These segments were identified and removed manually when the profiling speed deviated from the median value by more than ± 1.5 times the standard deviation. Secondly, large amplitude, short-duration spikes were eliminated from the shear data using the despiking algorithm provided in Rockland's ODAS Matlab Library (v4.4.06). In particular, spikes were identified using a threshold value of 5 when comparing the instantaneous shear signal to a smoothed version. The smoothed signal was obtained using a first-order Butterworth filter, with a cut-off frequency ranging from 0.7 to $0.9\,\text{Hz}$, depending on the median value of the fall speed. Once identified, spikes were removed over a $5\,\text{cm}$ segment (ca. 0.07 s). Thirdly, the shear signals were high-pass filtered at $1.5\,\text{Hz}$ to remove low-frequency contamination (0.1 - $1\,\text{Hz}$) that is believed to be associated with the pyroelectric effect. The spectrum of the high-passed vertical shear signal was computed and used to estimate the dissipation rate (see below). The low-frequency portion of the signal, i.e. Sh_{LP}, from shear probe 1 was also analyzed (see Appendix).

2.6 *In-situ* dissipation rate and mixing

The dissipation rate of turbulent kinetic energy (TKE) was calculated using the isotropic relation $\epsilon = 7.5\nu\langle(\frac{\partial u}{\partial z})^2\rangle = 7.5\nu\langle(\frac{\partial v}{\partial z})^2\rangle$, where ν is the kinematic viscosity of seawater and u and v are the horizontal components of the small-scale velocity fluctuations. In practice, the estimate of ϵ was obtained iteratively by integrating the shear spectra up to an upper wavenumber limit ($k_{\max}$), i.e. $\epsilon = 7.5\nu\int_0^{k_{\max}}\phi(k)dk$ as is outlined in Rockland's Technical Note 028 (Lueck [2016]). This was done for each microstructure sensor separately, i. e. for du/dz (as sh_1) and dv/dz (as sh_2). The shear spectra, and hence dissipation rates, were estimated using the ODAS Matlab Library (v4.4.06).

337 Dissipation segment lengths of 3 s were used with 1 s fft-segments that overlapped by 50%.
338 The dissipation segments themselves were overlapped by ca. 1.5 s, which resulted in a
339 vertical resolution in ϵ of approximately 1.2 m. Contamination of the spectra for instru-
340 ment vibrations was reduced using the cross-coherency method of Goodman et al. [2006].
341 The quality of the spectra were assessed using a figure of merit, which is defined as $FM =$
342 $\sqrt{dof} \times mad$, where $dof = 9.5$ is the number of degrees of freedom of the spectra (Nut-
343 tall [1971]) and mad is the mean absolute deviation of the spectral values from the Nas-
344 myth spectrum as $mad = \frac{1}{n_k} \sum_{i=1}^{n_k} |\frac{\phi(k_i)}{\phi_{\text{Nasmyth}}(k_i)} - 1|$ where n_k is the number of discrete
345 wavenumbers up to $k_{\max}$ (Ruddick et al. [2000]). Segments of data where the spectra
346 had $FM > 1.5$ were rejected from further analysis. The final dissipation rate was ob-
347 tained by averaging the estimates for the two independent probes, i.e. ϵ_1 and ϵ_2 (respec-
348 tively from sh_1 and sh_2). If the values of ϵ_1 and ϵ_2 differed by more than a factor of 10,
349 the minimum value was used. FM values and Nasmyth's fit are included in the Fig. S1
350 of the Supplementary information. Probability distribution functions (pdfs) of ϵ were
351 computed with the Matlab Statistical Toolbox. Pdfs were obtained over various tempo-
352 ral and depth bins covering the physical domain of external forcings and vertical layers.
353 From ϵ we calculate the diffusion rate of turbulent kinetic energy K following the Os-
354 born relation (Osborn [1980]) as $K_\rho = \Gamma \epsilon / N^2$ with the mixing efficiency coefficient $\Gamma =$
355 0.2. To index the turbulent activity (Hebert & de Bruyn Kops [2006], Schultze et al. [2017]),
356 we use the buoyancy Reynolds R_{Eb} number derived from the ratio between the Ozmi-
357 dov scale L_O and the Kolmogorov scale L_K with $R_{Eb} = (L_O/L_K)^{4/3} = \epsilon/\nu N^2$ where
358 ν is the kinematic viscosity. The buoyancy Reynolds number can be interpreted as the
359 ratio of the maximum length at which eddies can overturn before being inhibited by buoy-
360 ancy to the length scale at which overturning is eroded by viscous forces (Gregg [1987]).
361 The study of Shih et al. [2005] indicates that fully turbulent isotropic mixing takes place
362 for $R_{Eb} > 100$, followed down then by the transitional regime $7 < R_{Eb} < 100$ in which
363 turbulence is not fully isotropic but able to mix the stratification anyway. A turbulent
364 activity index lower than $\sim 7-20$ indicates quiescent flow driven by molecular and buoyancy-
365 controlled regimes, not turbulent enough to generate an important diapycnal mixing (Ivey
366 et al. [2008], Bouffard & Boegman [2013]).

3 Results

3.1 Hydrology from the CTD profiles

369 The Gulf of Naples (**Fig. 1**) stands as a non-tidal coastal area in the Western Mediter-
370 ranean marked by a subtropical regime, and is directly affected by continental freshwa-
371 ter runoffs and salty water from the Tyrrhenian Sea. We present on **Fig. 2.a** the hy-
372 drology of the water-column during our survey. A clear seasonal cycle is visible : a strat-
373 ified period in July-August, followed by a progressive deepening of the MLD from Septem-
374 ber to November, that finally reaches a period when the water-column can be consid-
375 ered as fully mixed, from December to February. From the surface down to 50-60 m depth,
376 relatively fresh waters persist all along the summer till early November after which they
377 are rapidly replaced by salty waters that remain till the end of the record (**Fig. 2.a**).
378 A salty bottom layer of 38.1 to 38.3 g kg^{-1} is visible below the 28.3 kg m^{-3} isopycnal layer
379 all along the record. As for the general pattern of the Brunt-Väisälä frequency N^2 (**Fig.**
380 **2.b**), a strongly stratified, 10 m thick transitional layer is observed below the MLD, sep-
381 arating the surface from the internal and bottom layers (Johnston & Rudnick [2009]).
382 We make the hypothesis that internal wave breaking is among one of the processes that
383 lead to intensified dissipation rates, and propose to analyze the stratified layers below
384 the MLD by decomposing them vertically through the two first baroclinic modes (B1 and
385 B2 respectively) that we presume containing most of the energy of the internal oscilla-
386 tions (see Supplementary information S2). The determination of their vertical extension
387 was made for each profile by identifying the depth ranges containing the shear maximum
388 values. The maxima of B1 are located immediately below the MLD and are associated

389   with the highly stratified part of the water column, while the maxima of B2 lie deeper
390   and are associated with a weaker stratification (see supplementary Fig. S2). Finally, the
391   water column between B2 and the bottom was considered as a separate layer. We present
392   the vertical extension of the vertical bins in **Fig. 2.c**. This partitioning was then used
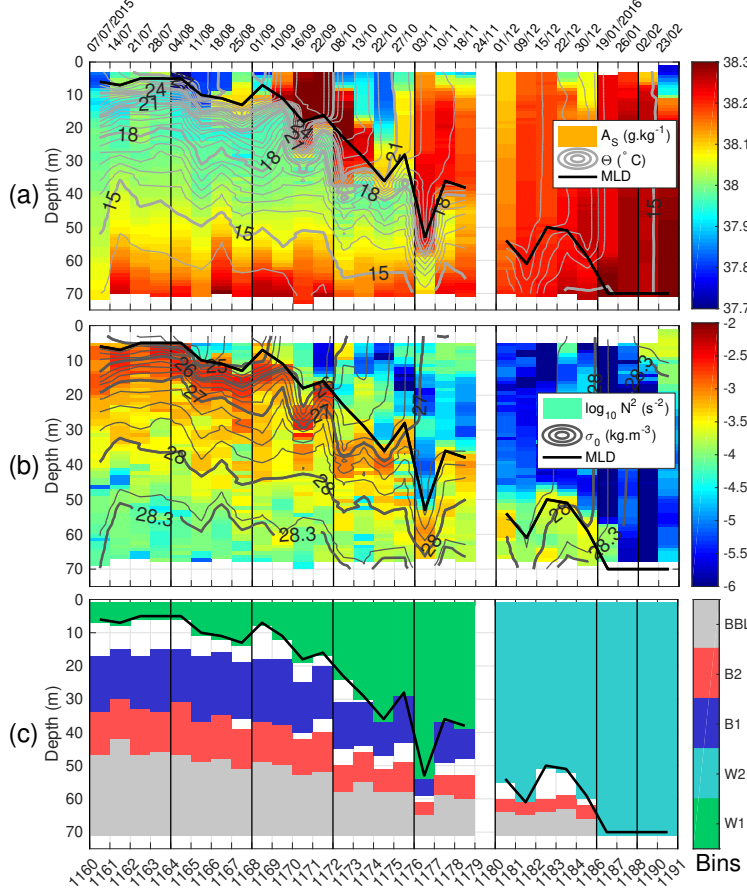393   for the statistical characterization of the de-stratification.

Figure 2: CTD `SBE-911+` profiles. (a) Absolute Salinity A_S $(\mathrm{g\,kg^{-1}})$ with contours of
Conservative temperature Θ (°C). (b) Brunt-Väisälä frequency N^2 $(\mathrm{s^{-2}})$ and contours
of potential density σ_0, plotted from 24 to 27 $\mathrm{kg\,m^{-3}}$ every 0.25 $\mathrm{kg\,m^{-3}}$, with the 28.3
$\mathrm{kg\,m^{-3}}$ isopycnal emphasized in thick black near the bottom. (c) Vertical and temporal
bins used thereafter for the statistical characterization by periods and layers : surface to
MLD during the summer to autumn period $W1$ (green), surface to MLD during the win-
ter period $W2$ (cyan), the vertical layer of the shear maxima of the first baroclinic mode
$B1$ (blue) and second baroclinic mode $B2$ (red), and the bottom boundary layer BBL
(gray). (All) $MLD_{\theta_0}^{0.4°C}$ (thick black line). X-axis indicates the sequence of MC-CTD
profiles references, and sampling dates are given on the panel top.

3.2 Wind, waves, and buoyancy forcings

3.2.1 A seasonal overview

The time evolution of buoyancy fluxes, surface winds and waves is investigated to look for possible impacts on the deepening of the MLD. Here we point to the reader that we show daily mean values, estimated by averaging from midnight of one day to midnight of the next day, and these smoothed values can be misleading when comparing them to the 6-hours values as we will do when looking to the casts with more details (see subsection 3.2.2 thereafter). In general, positive buoyancy fluxes strengthened the stratification of the water column while negative buoyancy fluxes weaken the stratification and may lead to surface convection and deepening of the MLD. During summer and till mid-September, the daily averaged B was always positive apart from three short episodes of negatively buoyant days (**Fig. 3.a**, gray line). In contrast, after mid-September B remained negative (or close to zero). Consequently, from the beginning of the observed period, the cumulative buoyancy flux increases and reaches a maximum level around mid-September and then constantly decreases from mid-October to reach a minimum at the end of the record (**Fig. 3.a**, gray dashed line). The contribution of heat (B_T) and freshwater (B_S) fluxes to daily buoyancy fluxes clearly show that B_T dominates, being larger than B_S by one order of magnitude except during rain events (**Fig. 3.a** and **Fig. 3.b**, blue lines). Precipitation rates shows intermittent events with values larger than 20 mm d^{-1}, with a maximum of about 70 mm d^{-1} in early October, followed by intermittent rainy events during the rest of the period. During those events, (positive) B_S became comparable to B_T (**Fig. 3.a**, solid pink blue and gray lines). Note that without measurements of the river runoffs contribution, there were not accounted for despite they are likely of importance over this coastal area (the Sarno river runoff into the Gulf of Naples is about $13 \text{ m}^3 \text{s}^{-1}$, while the Volturno river runoff into the Gulf of Gaeta is about $82 \text{ m}^3 \text{s}^{-1}$ (Albanese et al. [2012])).

Buoyancy fluxes counteract the wind stresses, which are able to mechanically mix the surface layer and contribute to the deepening of the MLD. The wind stress (**Fig. 3.b**) over the summer period is weak and shows few intermittent events before the mid-September (MC1171) with $u_*^3 < 0.5 \times 10^{-6} \text{ m}^3 \text{s}^{-3}$. Stronger energetic storms with values $> 1.5 \times 10^{-6} \text{ m}^3 \text{s}^{-3}$ occurred two months later, around the 20th November, followed in January and February by other stormy periods. To identify the direct contribution of the wind to the mixing within the water column, we calculated the Monin-Obhukov length scale (see Methods) to characterize the dominance of wind stress over positive buoyancy fluxes. Unrealistically large values (i.e. $|L_{MO}| > 100 \text{ m}$) have been discarded. Note that, because strong winds prevented any ship observation during storms, the MLD was only diagnosed after (and not during) the occurrence of extreme events, inhibiting a detailed analysis of covariance between MLD and L_{MO} during stormy periods. We show on **Fig. 3.c** (gray dots) cases when wind mechanical forcing was responsible for the MLD deepening. During the stratified period, the L_{MO} remained in the range of $0.01-1 \text{m}$, that is, the winds were too weak to break the stratification and thus to deepen the MLD (MC1160 to MC1170 included, from July to mid-September). Strong values of $u_*^3 > 0.5 \times 10^{-6} \text{ m}^3 \text{s}^{-3}$ occurred after MC1171, after which the L_{MO} regime shifted toward values O(10 m) until MC1177 included (mid-November). The strong event of $u_*^3 > 2 \times 10^{-6} \text{ m}^3 \text{s}^{-3}$ of the end of November between MC1178 and MC1179 marked the start of the winter period, with values of L_{MO} reaching values $> 10 \text{ m}$ between MC1184-MC1186 and MC1188-MC1190. Most of the MLD deepening occurs during the period from late-summer to winter. Despite this period is characterized by negative B, our analysis cleary shows that wind forcings dominates over B (**Fig. 3.c**, purple points) rather than the opposite (dark blue dots). Thus, the MLD deepening is mostly induced by wind mechanical mixing. Cases with no significant wind conditions occurred mainly in December, with some additional short events in October and November. This change of the main atmospheric forcings properties over the seasons led us to split the analysis of two temporal periods : $W1$ from MC1160 to

447     $MC1178$ (July to mid-November), and $W2$ from MC1179 to MC1190 (end of November
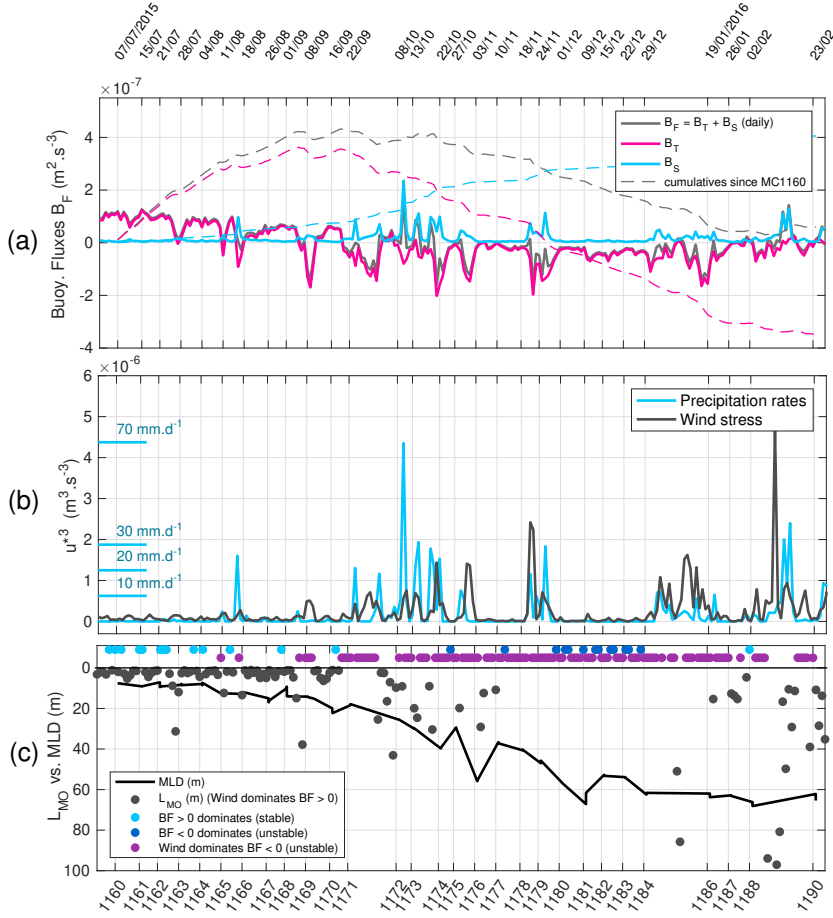448   to February), respectively (**Fig. 2.c**).

Figure 3: (a) Daily averaged buoyancy fluxes B (m^2 s^{-3}). Gray line indicates the sum of heat and freshwater contributions B_T (solid pink) and B_S (solid blue). The associated dashed lines indicate the cumulative values from the 7th of July 2015 (scaled down by a factor 10 for graphical purposes). (b) Daily averaged precipitation rates P (mm d^{-1} in blue) and wind stress u_*^3 (m^3 s^{-3} in gray). (c) MLD (solid black) and Monin-Obhukov length scale L_{MO} (m in gray dots) during stable buoyancy fluxes. On the horizontal line near surface, dots indicate the occurences of the other regimes (stable in light blue, unstable dominated by negative fluxes in dark blue, and unstable fluxes dominated by wind stress in purple). X-axis indicates the MC-CTD casts references. Sampling dates are given on the panel top.
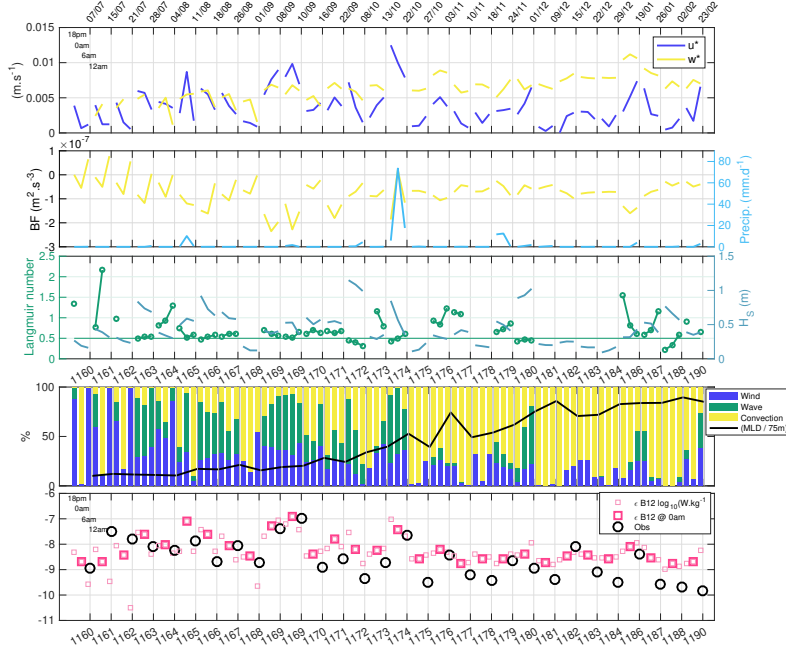
Figure 4: (a) Wind stress u_* (m s^{-1} in blue) and convection velocity scale w_* (m s^{-1} in yellow) plotted before each cast at 18 pm of the previous day, 0 am, and 6 am (time of MC cast is approximated to be at 12 am). (b) Buoyancy fluxes (m^2 s^{-3} in yellow) and precipitation rates P (mm d^{-1} in blue). (c) Langmuir number (no units, in dark green, the horizontal line indicates a threshold value of 0.5) and significant wave height H_S (m in light green). (d) Relative contribution between wind (blue), wave (green) and buoyancy (yellow) forcings to the modelized value ϵ_{B12} (showed on (e)). Black lines indicates the mean MLD (% of the 75-m bottom depth). Note that for each cast MLD is plotted at noon. (e) Dissipation rates of turbulent kinetic energy (W kg^{-1} in log$_{10}$) for the model B12 (light pink squares at 18 pm, midnight, 6 am, and thick pink at midnight) and VMP observations at $z = MLD/2$ (black circles), averaged arithmetically between the different profiles of the same cast. X-axis indicates the MC-CTD casts, presented in sequence without temporal gaps. Sampling dates are given on the panel top. Time of casts is considered to be close to noon, and forcing estimates are showed during the 16 previous hours, at 18 pm of the previous day, midnight and 6 am.

3.2.2 Forcings during the 16 hours before the casts

In this sub-section we propose to show the wind, wave, and buoyancy forcings in a temporal window before each MC cast **(Fig. 4)**. As it will be discussed in the Section 3.5 dedicated to ϵ, a significant agreement between ϵ_{B12} and ϵ_{VMP} is obtained when comparing the observations in the middle of the MLD to the model estimated from the forcings seen at midnight during the night, before the MC casts, close to the time response of $\sim$ 12 hours in the study of Lozovatsky et al. [2005]. This motivates to present a focus over the 16 hours period that occurred before each cast, at 18 pm (the day before), midnight, and 6 am. The periods identified previously in the seasonal overview are now depicted with more details. It is noteworthy that if looking at the casts with a temporal window of 16 hours, without gaps between casts, intense events of precipitation rates that happened between casts are not visible, except for the intense case of MC1174 with a peak of around 85 $\mathrm{mm\,d^{-1}}$ at midnight (leading to a stable B at 0 am), or the casts MC1165 and MC1179 with more moderate values around 10 $\mathrm{mm\,d^{-1}}$ (blue line on **Fig. 4.b)**. In general we can see a moderate negative nocturnal B, and weak wind ($u_* < 0.005$ $\mathrm{m\,s^{-1}}$) for MC1160 to MC1162, followed by a negative B and moderate wind ($u_* \approx 0.05$ $\mathrm{m\,s^{-1}}$) for MC1163-1164, and MC1166-1167 (July to August). An intensification at 0.008 $\mathrm{m\,s^{-1}}$ is seen at MC1165 (August), while a weakening occurs ($u_* < 0.002\ \mathrm{m\,s^{-1}}$) at MC1168 (September). Then both intense wind and negative B at MC1169 (in September). Note that the same cast is realized on two different (close) dates (see supp. Tab S1). While La was in general close or larger than 0.5 from MC1160 to MC1171, the situation changes in the periods before the cast MC1172 and MC1174 (October), then MC1180 (December) and MC1188 (February) with a decrease showing values of $La\ <\ 0.5$. This suggest a contribution of wave-forced turbulence in the MLD at these periods.

3.3 Turner's regimes : diffusive convection and double diffusion

The seasonal variability we observed is associated with large variations of the thermohaline vertical gradients that may drive various regimes of stability. We quantify those different regimes through the study of Turner's angles, estimated from the relative contribution of vertical gradients of salinity and temperature (Section 2.2). There is a clear partition of the stability between diffusive convection and salt fingering regimes at the MLD **(Fig. 5.a)**. In the fall and winter months, the diffusive convection regime occupies the region above the MLD, whereas in the summer months the salt-fingering regime is present beneath the ML. More complete statistics of the Turner angles are presented in supplementary Tab. S2.

Diffusive convection regime is observed locally with patchy structures that appeared in August at the surface, followed by larger ones in October, between 10 and 30 m . This situation repeated in December, although the vertical distribution of this regime is more variable. Below the ML, a pattern of double diffusive regime is visible, driven by warm and salty water overlaying on the relatively colder and cooler layers. The period from mid-September to November presented layers prone to salt-fingering that were located below the local maximum of salinity of 38.2 $\mathrm{g\,kg^{-1}}$. The periods $W1$ (late summer and fall) and $W2$ (winter) presented differences in the intensity of the diffusive regime, with median intensity of $Tu \approx -45°$ and $R_\rho \approx 0.33$ during $W1$, weaker in term of instability than for $W2$ showing median values $Tu \approx -72°$ and $R_\rho \approx 0.5$. Diffusive layer (DL) is presumed to occur when the values of R_ρ^{-1} are 1.0 - 3.0 (Carniel et al. [2008]), and that is what we observe here.

In terms of salt fingers, the regime observed in the ML during the destratification shows a median value of $Tu \approx 59°$ and $R_\rho \approx 3.8$, which is out of the active range ($R_\rho \approx 1.0$ - 3.0) but more intense than the regime found below the MLD (median $Tu \approx 50°$ and $R_\rho \approx 8.4$). Making the assumption that these SF layers are close to be active (characterized by $R_{Eb} < 20$ on **Fig. 5.e**, see Nakano et al. [2014], or Vladoiu et al. [2019]),

and following the parameterization of salt fingers processes (Carniel et al. [2008] (Eq. 2), J. Zhang et al. [1998], Inoue et al. [2007], Onken & Brambilla [1029]), we obtain salt and thermal diffusivities K_S and K_θ, respectively of around 5.5×10^{-7} and 1.0×10^{-7} m^2 s^{-1} in function of $R_\rho = 3.8$,

To compare to the turbulent kinetic energy diffusivity, we apply the parameterization from Nakano & Yoshida [2019] (Eq. 8) $K_\rho^{\text{SF}} = (K_T^{\text{SF}} R_\rho - K_S^{\text{SF}})/(R_\rho - 1)$ and obtain a negative value (-5.9×10^{-8} m^2 s^{-1}) indicating that SF reduces the potential energy of the system and intensifies density stratification [Nakano & Yoshida, 2019]. From the VMP dissipation rates estimates, the mean values of the momentum diffusivity in these locations are around 1.2×10^{-5} m^2 s^{-1} in the ML during W1 and W2, and 5.7×10^{-6} m^2 s^{-1} below the MLD in the SF layers (**Fig. 5.d**). Despite their presence in the coastal area, here double-diffusive seem to contribute weakly to the water-column turbulent mixing, as it was expected in weakly turbulent environments as pointed by the work of Lenn et al. [2009].

3.4 Turbidity observations

The seasonal variability of vertical mixing is associated here with some patterns visible in the turbidity measurements of the JFE Advantech Co. fluorometer-turbidity sensor mounted on the `VMP-250` (**Fig. 5.b**). These data indicate a turbid bottom layer co-located with the deep salty layer (**Fig. 2.a**). When the ML reaches the proximity of the bottom, from the end of October to December, some turbid bottom patches are visible (MC1175 on the supplementary Fig. S3.b, or MC1180 on Fig. S3.c). This provides evidence of the re-suspension of sediments in a non-tidal area, by energetic processes located between the MLD and the bottom boundary layer, as observed in the study of Masunaga et al. [2015] in a shallow bay where distinct nepheloid layers were produced by internal bores leading to breaking internal waves, and studied in Haren et al. [2019]. In general, processes of re-suspension due to bed shear stress by wind, waves and currents could be investigated (Green & Coco [2014]). Once a full vertical homogenization is achieved in January (the core of winter period), no additional turbid layers are observed. Looking at the subsurface, local turbid patches are present inside the ML from September to November, with structures occupying a large part of the water column (MC1179 on **Fig. 5.b**). This depicts the complexity of the winter mixing at the coastal area, underlying the possible important role of the runoffs discharging sediments at various point of the coast after rainfalls (López-Tarazón et al. [2010]), and of the mesoscale features laterally advecting them from the shelf to the open basin (Washburn et al. [1993], O'Brien et al. [2011]).
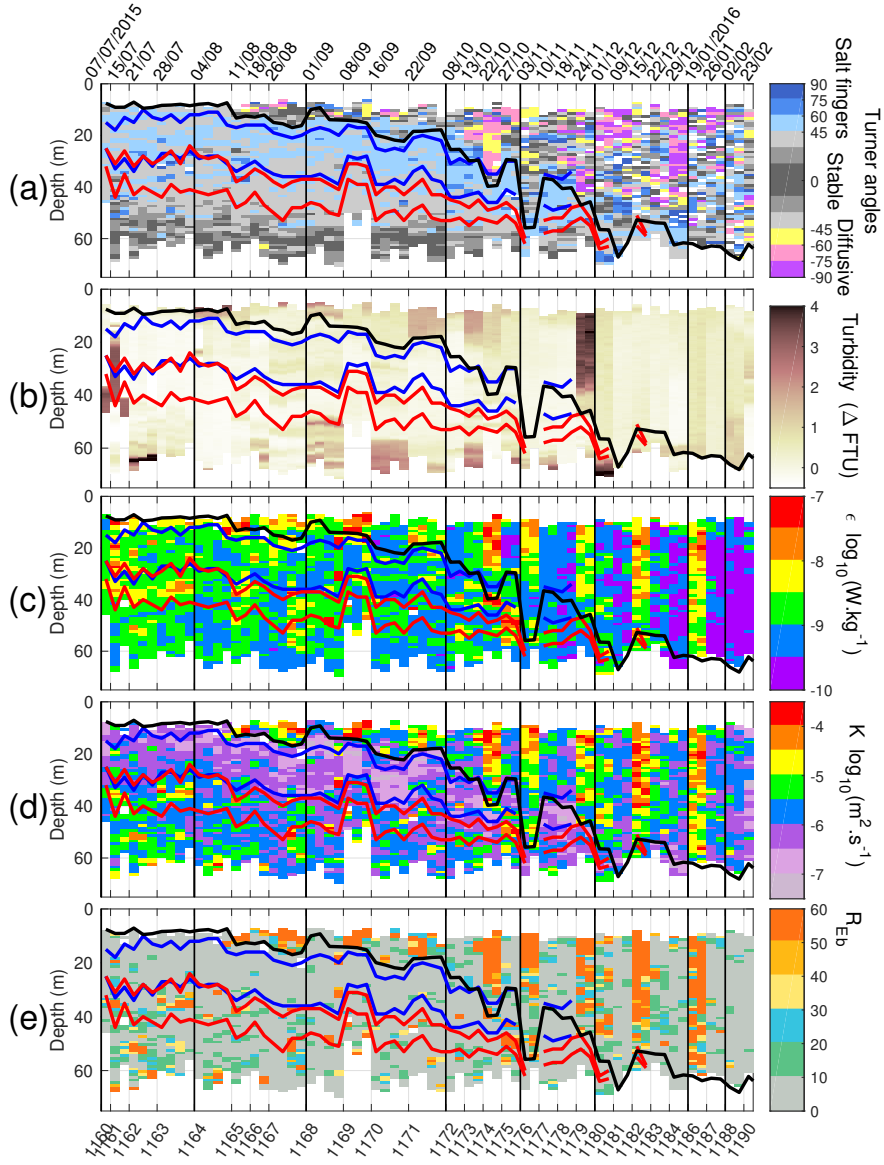
Figure 5: `VMP-250` profiles, plotted sequentially (x-axis does not represent time). (a) Turner angles (angular °), (b) Turbidity (ΔFTU) (Formazin Turbidity Units, offset from a reference value), (c) Dissipation rate ($W\,kg^{-1}$), (d) Diffusion rate ($m^2\,s^{-1}$), and (e) buoyancy Reynolds number. (All) $MLD_{\theta_0}^{0.4°C}$ (thick black), region of maximum energy of baroclinic mode 1 (between blue lines) and mode 2 (between red lines). The VMP profiles are plotted sequentially along the x-axis, where the MC casts references are indicated (from one to four VMP profiles by cast). Sampling dates are given on the panel top.
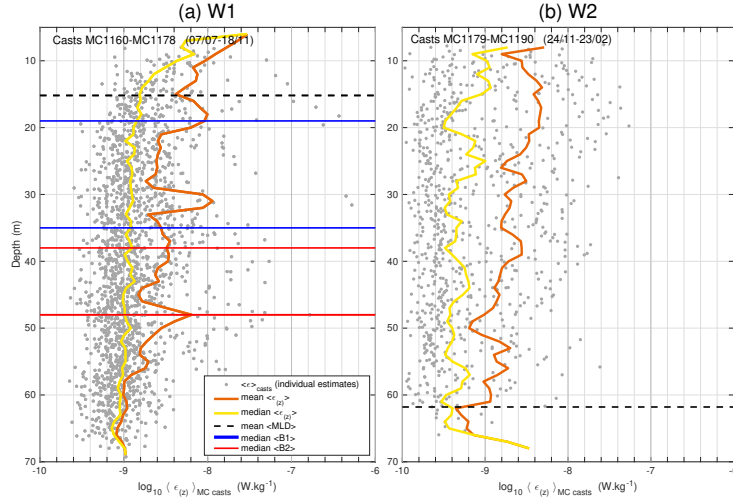
Figure 6: Mean (orange) and median (yellow) profiles of ϵ (W kg^{-1}), from arithmetic averaging, over the (a) summer-fall period W1 and (b) winter period W2. Gray background points are individual ϵ estimates. Horizontal dashed lines indicates the median depths of the MLD (black) and the upper and lower depths of B1 (blue) and B2 (red) during the stratified period $W1$.
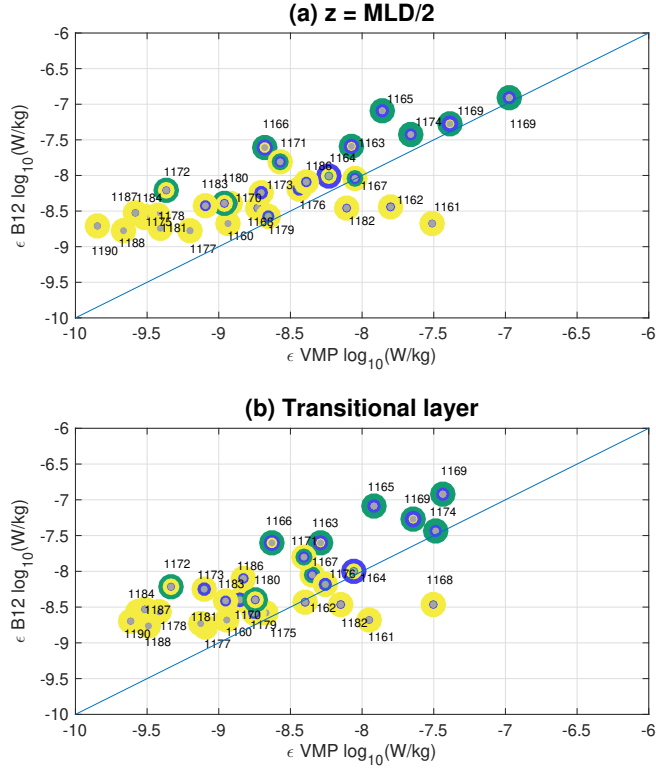
Figure 7: Scatterplot between the model ϵ_{B12} and VMP observations taken at (a) $z = MLD/2$, and (b) the transitional layer (MLD to the upper depth of B1). For VMP, unique value for each cast are obtained by averaging arithmetically the observations between repeated profiles in the same cast and layers. Thickness of colors refer to the contribution of wind (blue), wave (green), and convection (yellow) to the estimate of ϵ_{B12}, with the respective percentages given on Fig. 4
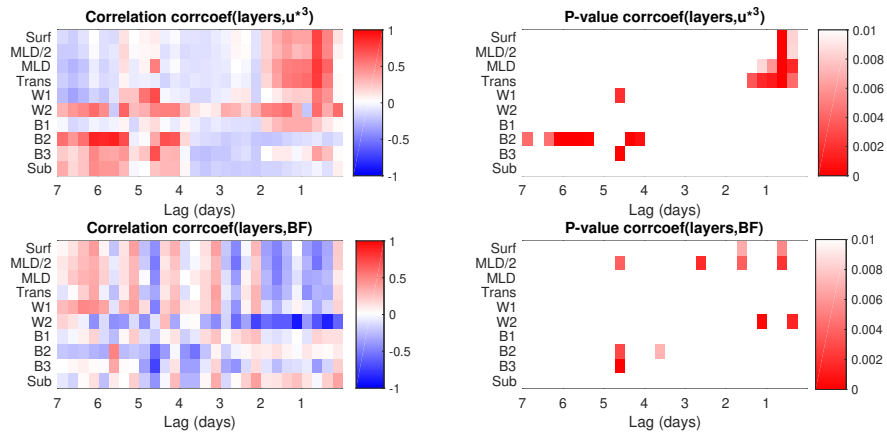

Figure 8: Coefficients of correlations between ϵ and u_*^3 (Top), and buoyancy fluxes B (Bottom), by layers of interest and for lags of 6 hours until 7 days in the past.

3.5 Observations of turbulent kinetic energy dissipation rate ϵ

The seasonal sequence of vertical profiles of dissipation rates of turbulent kinetic energy shows maximum values between 10^{-8} and 10^{-7} W kg^{-1} (**Fig. 5.c**), distributed through patches in various parts of the water column. For a given station, ϵ varies within a factor of five between the successive casts done typically within one hour (e.g., stations MC1163, MC1168, or MC1171). The summer period shows values of 10^{-8} W kg^{-1} at the depth-range of the MLD, around 10 m. The most intense patches are from 5×10^{-7} to 10^{-8} W kg^{-1} between 20 and 35 m in July (MC1160 to MC1163), then between 35 and 50 m in August and September (MC1164 to MC1171). They match the MLD depth in October (MC1174 and MC1175). Minimum values of 10^{-10} W kg^{-1} are measured, which are near the noise limit of the instrument. In winter, the dissipation rates are low throughout most of the water column (MC1184, MC1188, MC1190). The turbid patches identified previously are associated with local patches of ϵ from August to January, with values from 10^{-8} to 10^{-7} W kg^{-1} in surface from 10 m to around 20 m (MC1165, MC1171, MC1174), and in the lower range of around 10^{-9} to 10^{-8} W kg^{-1}, into the water column (MC1179, MC1186) or at the proximity of the bottom (MC1168, MC1173). Profiles of ϵ are grouped by their mean and median values over the stratified period $W1$ and winter period $W2$ (**Fig. 6**). During $W1$, the median profiles converge from 10^{-8} to 10^{-9} W kg^{-1} from 10 to 25 m, and then remains around 10^{-9} W kg^{-1} down to the bottom, punctuated by local intense values $> 10^{-7}$ W kg^{-1}. Layers below the ML show intermittent local maximum values reaching 10^{-8} W kg^{-1}, located in the vertical between region of the two first baroclinic modes maximum. The winter period $W2$ shows a tendency of $\langle \epsilon \rangle$ values to be centered around 10^{-10} and 5×10^{-8} W kg^{-1} (**Fig. 6.b**). Peaks are observed at various depths in the water-column, marking both spatial and temporal intermittency. They are more pronounced in the stratified layers, which may underline that intermittency is stronger in these locations. It should be noted that our observations were made when weather conditions were favourable for a safe deployment of the VMP-250, sometimes after energetic storms but certainly never during storms. Therefore, the most intense turbulent events are likely missed.

We split the overview of ϵ by looking separately at the mixed and stratified layers. We show there the comparison between observations and model. To relate ϵ to wind stress and buoyancy forcings, we propose to explore the correlations between times series of ϵ and u_*^3 and B, by layers and with introducing lags of 6 hours to identify possible temporal responses. Then, to characterize the distributions of ϵ, we apply then the same framework as Lozovatsky et al. [2017]. We present in **Fig. 9** the empirical probability density function (pdf) of ϵ and N^2 on the two forcing periods W1 and W2, and differentiate the surface from the internal and bottom layers B1, B2 and BBL (see **Fig. 2.c**).

3.6 ϵ in the surface layer

We compare ϵ_{VMP} and ϵ_{B12} in the surface layers. The model proposed by Belcher et al. [2012] allows to interpret ϵ values as a linear combination of the contribution of wind, waves, and buoyancy forcings, and their estimation of ϵ is defined at the *depth at which the three type of turbulence are well developed*. To achieve this, Sutherland et al. [2014] compared with good agreement the model to observations taken at the mixing layer depth and at $z = MLD/2$. We used the latter and confirmed the general agreement between ϵ_{B12} and ϵ_{VMP} (see **Fig. 7.a**), with the most significant correlations (0.8380, with a p-value of 7.6027×10^{-9}) obtained when evaluating ϵ_{B12} with the forcings taken at midnight during the night before each cast. Observations were made between 8 am and noon, and this results confirms the mean delay of adjustment of $\sim 10 - 12$ hours for the stratification to respond to forcings, as showed by Lozovatsky et al. [2005]. We use the model to interpret the relative dominance of forcings that led to dissipation. Looking on **Fig. 4.e** at the partition during time, W1 (MC1160-MC1178) marks a progres-

sive transition of the dominance of wind and waves to buoyancy forcings. During W2 (MC1179-MC1190), nocturnal convection dominates the wind, with some cast (MC1179, MC1180, MC1188) suggesting a contribution of the waves. In general, model appears to be closer to observations when all wind, waves, and buoyancy forcings were present during the stratified period (MC1160-MC1174). Outliers (see MC1161, MC1166, MC1172 on **Fig. 4.e**) could be due to consider the forcings with the wrong respective lag. During the winter period, estimates are dominated by convection, and/or we suppose that wind and waves were less well represented, and application of the model may be less consistent. The pdf for the surface bins (**Fig. 9.a**) shows values around 4×10^{-10} W kg^{-1} for W1, and 2×10^{-10} W kg^{-1} for W2, the latter being dominated by stronger winds and negative buoyancy fluxes. Both distribution are well fitted by a Burr type XII, and differ from log-normality. Regarding the stratification (**Fig. 9.b**), the summer to fall period shows a distribution centered on 5×10^{-5} s^{-2} (W1 in green), while winter is characterized by a distribution centered on 3×10^{-5} s^{-2} (W2 in cyan).

3.7 ϵ below the MLD

If we interpret the deepening of the MLD as a process resulting of mixing events happening both in the surface mixed layer and in the stratified layers below, the transitional layer becomes of interest to understand the variability of the MLD. Interestingly, another good correlation appears (0.6845, with a p-value of 3.0287×10^{-5}) when taking in account the transitional layer below the MLD to the top of the layer of the first baroclinic mode (B1), suggesting a good representation by the model of the response in dissipation to the external forcings into this specific layer. Below the mixed layers (**Fig. 9.c**), the pdf of ϵ shows a dominant peak centered on 5×10^{-10} W kg^{-1} for B1, and on 9×10^{-10} W kg^{-1} for B2. The distribution within the BBL (**Fig. 9.e**) is narrower compared to B1 and B2, and shows a dominant peak centered on 7×10^{-10} W kg^{-1}. The observations are better described by the Burr type XII distribution than the log-normal, even if the deviation from log-normality is not so pronounced than for the distributions of the surface bins W1 and W2. Regarding the N^2 below the ML (**Fig. 9.d**), the pdf in B1 is centered around 4×10^{-4} s^{-2} and close to log-normality. The distribution in B2 is more variable, with values spread in the range 2×10^{-5} to 3×10^{-4} s^{-2}, making difficult to distinguish which distribution fits better. Similarly, in the BBL (**Fig. 9.f**) values are spread in a wide range (3×10^{-5} to 2×10^{-4} s^{-2}), with a central peak at 7×10^{-5} s^{-2}, making it difficult to define a best fit between Burr and log-normal distributions. Details of statistics are given in **Tab. 1.a,b**.

By making the hypothesis that internal waves are present in the stratified layers, that their generation is made continuously since the initial energy input, and that their intermittent breaking should sign in our observations of ϵ, we investigated lagged correlations between the time series of ϵ in the baroclinic layers, and the wind stress and buoyancy fluxes at surface, from the moment of the cast up to 7 days in the past, every 6 hours. Cases of significant auto-correlation for u_*^3 and BF are not considered (from 0 to 2 days for B, and around 3 days for u_*^3). Additionally we don't investigate lag time close or overlapping the main duration between cast (generally from 6 to 9 days, or more). Correlations with the significant p-values are presented on **Fig. 8**. In general we reproduce well the correlation found with the model taken at midnight (the first lag is considered 0-lag and associated to noon that we consider the closest to the cast hour, the second being associated to 6 am, and the third to midnight). Compared to wind stress, the transitional layer appears to respond during more than one day. Interestingly B2 is showing correlations at around 4.25 days, and from 5 to 6 days. The lagged correlation with B are more noisy, probably contaminated by the strong daily cycle, but it shows anyway correlation with negative B the 24 hours before the casts during W2, and between 4 and 5 days in the B2 layer. Such time scale opens the question of the mechanism that should be able to delay, or progressively transfer the energy injected at larger

639   scale, and ϵ observed should consequently be associated to both short (~ 12 hours) and
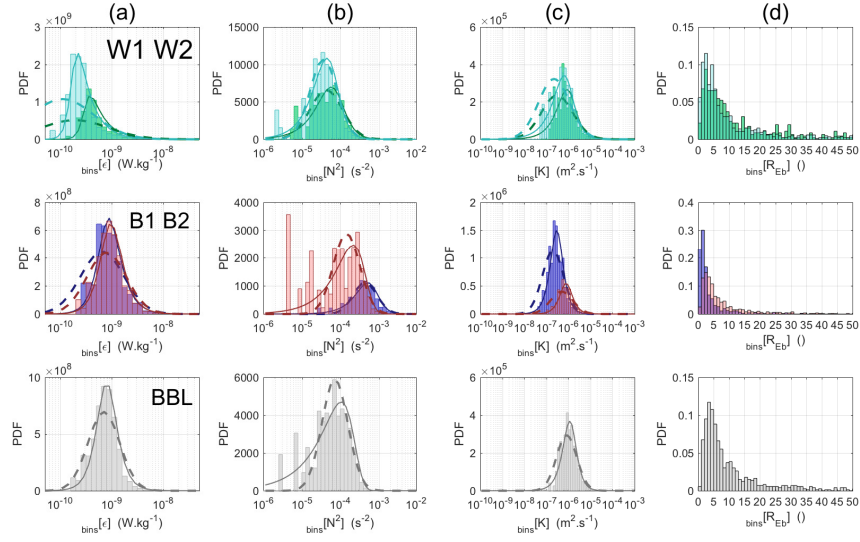640   intermediate time scales ($\sim 4 - 5$ days) .

Figure 9: PDFs of ϵ ($\mathrm{W\,kg^{-1}}$) (a), N^2 ($\mathrm{s^{-2}}$) (b), K ($\mathrm{m^2\,s^{-1}}$) (c), and buoyancy Reynolds number R_{Eb} (d), through temporal bins W1 and W2 (top), stratified layers B1 and B2 (middle), and near the bottom BBL (bottom). Fits of log-normal and Burr type XII distribution are indicated with the dashed and plain black lines, respectively. Bins are shown on Fig. 2.c, and detailed statistics are given in Tab. 1.

Table 1: Statistics of ϵ (a) and N^2, K and R_{Eb} (b). For both quantities are given general statistics by bins, and parameters for the fits of log-normal and Burr Type XII distributions, with their confidence intervals (c.i.). (c) Parameters of the quadratic fit $K = aS^2 + b$ of the $K = f(S)$. Parameters of the linear fit $\epsilon_{Obs} = f(\epsilon(B_12))$ at $z = MLD/2$ (d), and at the transitional layer (e).

(a) Statistics for ϵ

General

Bin	Population (Total 3084)	mean	median	skew.	kurt.
W1	372 (12%)	5.7×10^{-9}	1.1×10^{-9}	5.8	51.6
W2	771 (25%)	2.4×10^{-9}	4.1×10^{-10}	4.7	31.6
B1	561 (18%)	5.2×10^{-9}	1.2×10^{-9}	12.3	162.2
B2	379 (12%)	2.9×10^{-9}	1.3×10^{-9}	13.4	217.2
BBL	638 (21%)	1.5×10^{-9}	0.9×10^{-9}	7.1	67.7

Log-normal fit

Bin	mean	median	μ	[c.i.]	σ	[c.i.]
W1	4.9×10^{-9}	1.6×10^{-9}	-20.2	$[-20.4 - -20.1]$	1.5	[1.4 - 1.6]
W2	1.9×10^{-9}	0.7×10^{-9}	-21.1	$[-21.2 - -21.0]$	1.4	[1.3 - 1.5]
B1	2.4×10^{-9}	1.5×10^{-9}	-20.3	$[-20.4 - -20.2]$	1.0	[0.9 - 1.0]
B2	2.2×10^{-9}	1.5×10^{-9}	-20.3	$[-20.4 - -20.2]$	0.9	[0.8 - 0.9]
BBL	1.3×10^{-9}	1.0×10^{-9}	-20.7	$[-20.7 - -20.6]$	0.7	[0.7 - 0.7]

Burr XII fit

Bin	mean	median	α	[c.i]	c	[c.i.]	k	[c.i.]
W1	Inf	0.9×10^{-9}	0.3×10^{-9}	$[2.5 - 0.3 \times 10^{-9}]$	7.1	[5.0 - 9.9]	0.1	[0.05 - 0.11]
W2	Inf	0.5×10^{-9}	0.2×10^{-9}	$[1.5 - 0.2 \times 10^{-9}]$	6.8	[5.6 - 8.4]	0.1	[0.07 - 0.12]
B1	4.2×10^{-9}	1.2×10^{-9}	0.7×10^{-9}	$[6.5 - 0.8 \times 10^{-9}]$	4.0	[3.3 - 4.7]	0.3	[0.23 - 0.38]
B2	3.2×10^{-9}	1.3×10^{-9}	0.8×10^{-9}	$[7.1 - 0.9 \times 10^{-9}]$	3.9	[3.2 - 4.7]	0.3	[0.25 - 0.45]
BBL	1.4×10^{-9}	0.9×10^{-9}	0.7×10^{-9}	$[6.4 - 0.8 \times 10^{-9}]$	4.0	[3.5 - 4.5]	0.5	[0.37 - 0.57]

b) Statistics for N^2, K and R_{Eb}

Bin	mean N^2 (s^{-2})	median	skew.	kurt.	mean K (m s^{-2})	median	skew.	kurt.	mean R_{Eb}	median
W1	1.7×10^{-4}	0.9×10^{-4}	4.3	24.8	1.8×10^{-5}	2.8×10^{-6}	6.9	68.2	73.1	11.5
W2	0.9×10^{-4}	0.6×10^{-4}	5.3	58.9	1.3×10^{-5}	2.1×10^{-6}	8.0	100.8	45.9	7.3
B1	8.3×10^{-4}	6.4×10^{-4}	1.6	5.8	0.2×10^{-5}	0.5×10^{-6}	17.0	323.6	7.7	1.9
B2	3.0×10^{-4}	2.7×10^{-4}	2.2	13.3	0.6×10^{-5}	1.4×10^{-6}	5.6	289.4	19.1	4.7
BBL	1.5×10^{-4}	1.3×10^{-4}	1.0	4.2	0.8×10^{-5}	1.9×10^{-6}	26.9	728.6	26.1	6.6

(c) Quadratic fit parameters

	$K_\epsilon = f(S_\epsilon)$ $K = aS^2 + b$	$K_{N2} = f(S_{N2})$ $K = aS^2 + b$
Coeff. (with 95% conf. bounds)		
a	1.08 (0.85 1.31)	1.82 (0.89 2.75)
b	10.9 (-13.7 35.6)	1.30 (-12.95 15.56)
SSE	322.5	144.8
R-square	0.98	0.92
Adjusted R-square	0.98	0.90
RMSE	10.3	6.94

(d) Fit parameters at z = MLD/2

	$\epsilon_{\mathrm{obs}} = f(\epsilon_{\mathrm{B12}})$ $y = ax + b$	$\log_{10}(\epsilon_{\mathrm{Obs}}) = f(\log_{10}(\epsilon_{\mathrm{B12}}))$ $y = ax + b$
Coeff. (with 95% conf. bounds)		
a	1.121 (1.027 1.214)	0.4928 (0.3056, 0.6801)
b	2.376e-09 (2.75e-10 4.476e-09)	-3.95 (-5.574, -2.326)
SSE	7.239e-16	3.876
R-square	0.965	0.5095
Adjusted R-square	0.9637	0.4919
RMSE	5.085e-09	0.3721

(e) Fit parameters in the transition layer

	$\epsilon_{\mathrm{obs}} = f(\epsilon_{\mathrm{B12}})$ $y = ax + b$	$\log_{10}(\epsilon_{\mathrm{Obs}}) = f(\log_{10}(\epsilon_{\mathrm{B12}}))$ $y = ax + b$
Coeff. (with 95% conf. bounds)		
a	1.059 (0.8084, 1.31)	0.529 (0.2984, 0.7597)
b	2.328e-09 (-7.293e-10, 5.386e-09)	-3.651 (-5.644, -1.658)
SSE	1.292e-15	4.418
R-square	0.9375	0.4408
Adjusted R-square	0.9352	0.4208
RMSE	6.793e-09	0.3972

3.8 Relationships between observations

To complete the statistical characterization, we computed the skewness S and kurtosis K, which are indicators of the symmetry and the intermittency, respectively, of the observed variable (**Fig. 10.a**). The relationship between kurtosis K and skewness S of the different measured parameters was assessed by fitting a quadratic function $K = aS^2 + b$ for ϵ and N^2 (fit parameters can be found in **Tab. 1.c**). Additionally, theoretical curves for the log-normal and Gamma distributions are presented to allow for a comparison. Our statistics reproduce the same behaviour as in Lozovatsky et al. [2017]. The quadratic relationship fits well the dissipation rate observations (**Fig. 10.a**, squares over the black line) whose distribution is closer to the Gamma than to the log-normal distribution. Regarding the absolute values of the high order statistics, the stratified bins B1 and B2 are less symmetric and intermittent than for the surface bins W1 and W2, with the bottom bin BBL standing in between while being closer to the latter. Median values of ϵ (**Fig. 10.b**) indicate a partition between stratified and mixed layers, decreasing from 11×10^{-10} W kg^{-1} in the transitional period summer-to-fall ($W1$ in green) to 4×10^{-10} W kg^{-1} in winter ($W2$ in cyan). The strongest median values are around 13×10^{-10} W kg^{-1} and concern the stratified bins ($B1$ in blue, and $B2$ in red). In term of distribution, N^2 (**Fig. 10.a**) appear to be close to the log-normal distribution for the stratified bins (B1 in blue triangle, B2 in red, and BBL in gray), and differ in the mixed layers (W1 in green triangle and W2 in cyan). Its kurtosis (and skewness, not shown) clearly decreases in function of the intensity of the stratification (**Fig. 10.c**).
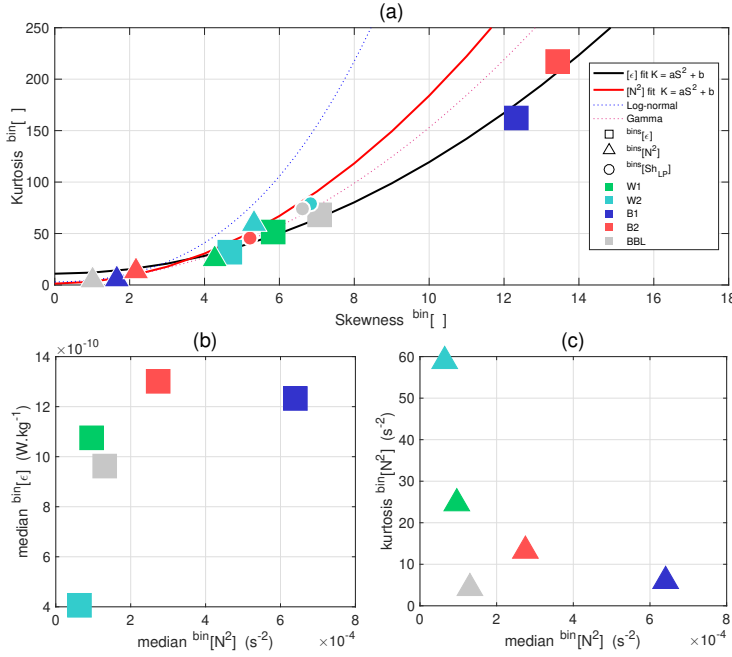

Figure 10: (a) Skewness (S) and kurtosis (K) of ϵ (squares), N^2 (triangles), and Sh_{LP} (dots), for the different temporal and vertical groups of data (colors refer to the bins on Fig. 2.c). A discussion dedicated to Sh_{LP} is given in the Appendix. Black and red plain lines indicate quadratic fits $K = aS^2 + b$ as proposed by Lozovatsky et al. [2017] and applied to ϵ and N^2. Statistics of the parameters can be consulted in Tab. 1. Blue and red dashed lines indicates theoretical curves for log-normal and Gamma distributions. (b) Median of ϵ (W kg^{-1}) and (c) kurtosis of N^2 (s^{-2}), in function of the median of N^2 (s^{-2}).

4 Discussion

General description of ϵ in the context of the stratification

We used CTD and microstructure observations to depict the time evolution of the water column in the Gulf of Naples, a mid-latitude non-tidal coastal site. This data set showed a deepening of the ML starting in late summer, marked by intermittent high dissipation rates below the MLD. Closer to the surface, we observed short periods of enhanced turbulence that may contribute to the deepening of the ML.

The shallow waters of the GoN are strongly influenced by the atmospheric forcings, synthesised schematically on **Fig. 11**, and we used the Monin-Obhukov length scale to overview the dominance of wind over positive buoyancy fluxes during the whole period. This allowed us to determine the different seasonal periods of forcings. Positive buoyancy fluxes in summer (**Fig. 11**, yellow arrow pointing down) maintain a strong stratification that light summer winds (**Fig. 11**, blue curly lines) can hardly break. Storms started at the end of summer with dominating enhanced wind episodes and the first negative buoyancy fluxes (**Fig. 11**, yellow arrow pointing up), both contributing to a deepening of the ML. Fall and winter periods were marked by increasingly negative buoyancy fluxes and few intermittent episodes of strong wind. Regarding the water column T-S properties, the close-by Sarno River, located in the northeast corner of the GoN (**Fig. 1**), is a potential source of freshwater anomalies propagating along the east side of the Gulf. This river could thus be the main source of the low salinity content of surface waters observed from July to October (**Fig. 11**, vertical dashed blue arrows) even if the study of Cianelli et al. [2012] showed that this influence should be constrained to the eastern part of the GoN. Satellite observations in recent studies of the regional circulations suggest an indirect influence of the Volturno river located in the Gulf of Gaeta (to the northwest and out of the GoN), whose nutrient-rich waters may reach the GoN through mesoscale and submesoscale features forced by the westerly wind events (Iermano et al. [2012]). A local pooling effect could exist in summer, with freshwater trapped at the coast by the daily oscillation of breeze winds (Cianelli et al. [2017]). The nearby Tyrrhenian sea instead acts as a source for the salty waters that were observed at depth from July to October, and over the whole water column later in the year (**Fig. 11**, dashed dark blue line). The key parameters is here the lateral salinity gradient across the location of the observations, that remains to be determined. These salty intrusions into the GoN are possibly at the origin of the salt-fingers patterns we identified and related to the the fine density steps we observed in our data set (**Fig. 11**, blue stairs). These steps-like features are present the coastal area, but manifesting on smaller scales than the typical Tyrrhenian stairs (Durante et al. [2019]). There, they may be related to interleaving events (Ruddick & Richards [2003]), and their vertical structure in layers of 0.3 to 3 m-thick is coherent with the case of a strong stratification and intermittent and weak mixing (Linden [1976], Turner [1983]). Double diffusive processes could be at the origin of a net transfer of mass toward the bottom layers and they could play an important role for the vertical transfer of nutrients available for biological species (Ruddick & Turner [1979]). The impact of salt-fingering on the duration of the stratified period remains to be quantified, even in such coastal areas where they are usually assumed to be insignificant. During the fall season, the unstable vertical salinity gradients progressively weakened, making subsurface layers more prone to diffusive convection (**Fig. 11**, yellow circles).

Mixing in the surface layers : which were the forcings ?

These upper layer processes that contribute to the ML deepening found their energy source in the atmospheric forcings. By applying the model of Belcher et al. [2012] taking in account the turbulence of wind, wave, and convection from bulk parameters, we confirmed the good agreement with observations at $z = MLD/2$, as shown by Suther-

land et al. [2014]. We found the best correlation when estimating the dissipation by the model when considering the forcings at midnight during the night before each cast. This confirms the assumption of Lozovatsky et al. [2005] that found a delay from 10 to 12 hours in the adjustment of the stratification to the wind forcings. To improve the use of the model, an investigation of the time scales associated to the forcings present in the temporal window of interest could be done to propose some temporal tuning for this method (e.g. applying various respective delays to the wind, wave, and convection terms). It is important to point that the model does not represent the turbulence associated with positive buoyancy fluxes (e.g. due to solar heating), therefore their contribution to ϵ is undetermined. Our observations were systematically made during the morning, from 8 am to 11 am, and if interpreted correctly, reflect the energy of the nocturnal forcings. The model takes in account the turbulence associated to the Langmuir regime, and our study confirm the importance to represent this process for a better estimate of ϵ in the surface layer (e.g. in numerical simulations), as it was pointed by the study of Lucas et al. [2019]. Estimates of ϵ were closest to observations for the cast where the contribution of the wave term was significant (roughly from 20 to 60 % of the whole assemblage with wind and convection). This suggest an important role for the Langmuir cells during the inter-seasonal period between summer and winter (**Fig. 11**, green circles).

Mixing in the stratified layers : indirect effect of surface forcings, and specific mechanisms of internal waves ?

Regarding the specific vertical structure observed in the GoN during the stratified period, with warm salty waters overlying cooler and fresher waters, salt-fingering can be active. We show that here their contribution to the diapycnal mixing seems to be relatively low, but their presence could provide a particular hydrological context for the generation, propagation and mixing of internal waves (Inoue et al. [2007], Maurer & Linden [2014]). Below the ML, the energy for sustaining the mixing is possibly brought by internal wave activity as the sheared layers suggest (**Fig. 11**, gray shaded layers). Locally, internal waves could also be generated by wind-driven deepening, supported also by Langmuir motions forced by the surface wave field (Polton et al. [2008], Lucas et al. [2019]). It is noteworthy that we did not sample during storms, which also act as local sources of internal waves. About this, the B12 model presents a good correlation with ϵ in the transitional layer, between the MLD and the upper depth of B1. The study of Lucas et al. [2019] about the stratification response to autumn storms concluded that in this layer ϵ was varying periodically at the local inertial frequency after the storm, due to enhanced wind shear alignment. This shear spike mechanism was introduced by Burchard & Rippeth [2009]. In shallow waters, in the presence of a bulk shear between the main flow and the bottom drag, some phase shift due to surface wind stress between upper and lower layers of the water column is likely important in enhancing the shear and lowering the Richardson number, consequently generating instability (Burchard & Rippeth [2009], Lincoln et al. [2016]). It is important to note that in coastal area influenced by freshwater inputs, this mechanism can be amplified by the straining of the stratification due to runoffs Verspecht et al. [2009]). Measurements of the large scale shear are planned for future cruises, as well as continuous measurements of horizontal gradients of temperature and salinity, to quantify the velocity field of the area, and determine the local characteristics of the bulk shear and horizontal density fronts. It is noteworthy that we found a significant correlation between time series of ϵ in the layer of the second baroclinic mode and the surface wind stress taken 4.25 days before the cast, suggesting that a mechanism delaying the energy injected into the system could be at work. Such time scale is compatible with the variability of mesoscale and submesoscale filaments that has been identified by satellite observations and modelization in the Gulf of Naples (Iermano et al. [2012]) The buoyancy Reynolds number was representative of quiescent flow below the MLD and in B1, suggesting a buoyancy-controlled in these layers (Bouffard & Boegman [2013]), while B2 (and the layer bottom below) is prompter to transitional regime,

with less wave damping by the stratification, and consequently more active to mix the stratification.

The proximity of the coast could play an important role in forcing internal waves, following the recent study of Kelly [2019]. They found that a coastal reflection of wind-driven inertial oscillations in the ML could generate offshore propagating near-inertial waves, associated to an intensified shear in the region below the ML (e.g. their Fig. 8). Indeed, the GoN coast is only 2 km away from the sampling site and we observed an intensification of shear events during the fall season, characterised by intense storminess and intermediate MLDs. Therefore, this specific mechanism could contribute to create these vertical shear events we observed in correspondence of the main baroclinic modes. In turn, this could contribute to the destratification of the water column during the transition to the winter state. The morphology of the GoN could be a source of internal waves generation too. Internal waves generated by current-topography interaction can radiate from the shelf to the coast with strong imprint on the first two baroclinic modes (Xie & Li [2019]). The existence of steep canyons in the GoN, and notably the Dohrn Canyon at south, provides a topographical configuration that could act as source for the generation of on-shore propagating waves. A current-topography interaction could be sustained also by the various bathymetrical features close to the coast (the Banco della Montagna, the Ammontatura channel and the Mt. Somma-Vesuvius complex on Fig. 1 in Passaro et al. [2016], located south, southwest and northeast from the LTER-MC sampling point). Finally, a recurrent transition of Kelvin coastal trapped waves over the area has been proposed in the numerical study by de Ruggiero et al. [2018].

What about the statistics given by our time series of ϵ ?

The oceanic response to climate change involves several processes, with various degrees of complexity. To reach a full predictive capability it is important to characterise their respective roles and the associated temporal and spatial variability. The analysis of the distribution of ϵ through the different periods represents a step toward a statistical characterization of ϵ, as investigated by the recent studies on the distribution in the interior ocean (Lozovatsky et al. [2017], Buckingham et al. [2019]). We showed that dissipation rates in the ML follows a Burr XII distribution instead of a lognormal. This result requires further study since a lognormal behaviour is considered as ubiquitous for such intermittent features (Pearson & Fox-Kemper [2018]). The respective roles of temporal intermittency and spatial heterogeneity remain to be determined. Finally, it is to note that the use of a small research vessel did not allow for sampling in rough weather and, therefore, the temporal intermittency is here presumably highly underestimated. This points to the need of microstructure observations that are designed to fully cover the spectrum of space and time scales (Pearson & Fox-Kemper [2018]). These specific challenges have to be met in the next future (Benway et al. [2019]) along with long-term observations to constrain the current climate change. Effort could include the deployment of microstructure devices mounted on moorings and wirewalker systems (Pinkel et al. [2011]), or to design and deploy dedicated drifters that regularly sample the water column as it is the case for the Argo floats (Roemmich et al. [2019]). In addition to following well-known probability distributions, we observed a quadratic relation between kurtosis and skewness in the statistics of ϵ, as it has been shown and discussed in the studies of Schopflocher & Sullivan [2005] and Lozovatsky et al. [2017]. This remarkable fit is quite universal since it does not depend upon the specificity of the physics's laws. It fits quite well also the low pass component of the microstructure shears, that was not used for estimating ϵ. In addition, the low pass shear events have a layer-averaged intensity that is linearly increasing with N^2. Statistics on the degree of intermittency, instead, are specific to the environmental conditions, that is, they are different for the ML and the interior.

Our microstructure survey was part of the long term monitoring of the coastal area of the GoN, by the Marechiara project started in 1984 and running until now. It provided an unique view, from July 2015 to February 2016, on the seasonal cycle of the stratification and mixing in the GoN. In the companion study in preparation, that investigated CTD and forcing data over 2001-2020, we derived the mean seasonal cycles of the water column structure. When compared to the bi-decadal mean cycles it is found that the water column in 2015 was fresher and accumulated relatively less heat, the late summer period being marked by significant rain event and moderate winds. In this study we observed that the long term thermal components (water column heat content, surface temperature) at the sampling site of the GoN did not exhibit increasing decadal trends as those observed over the Mediterranean basin (Pisano et al. [2020]), in contrary of the freshwater components reflecting the redistribution of precipitation at larger scale. So, in addition to a regional warming (e.g., heatwaves), the question of both the influence of larger scale actors (atmospheric systems changes) and intermittent events is to be considered (Baldi et al. [2006])). This promotes the efforts of long-term observations over these coastal areas to better understand the various processes and distinguish among them which ones (if not all) are more sensitive to future climate change. The complexity of mechanisms at finescales whose interplay produce convection, shear, mixing, leading to the ML deepening, can be significantly modulated by long-term heat, freshwater and wind changes (Somavilla et al. [2017]). In conclusion, we suggest that sites such as the GoN, a shelf region in a non-tidal area, are of interest for discriminating between processes less energetic than tides, as internal waves or even double-diffusion, beyond the global warming and the consequent increase of the stratification (Woodson [2018], Guancheng et al. [2020]).
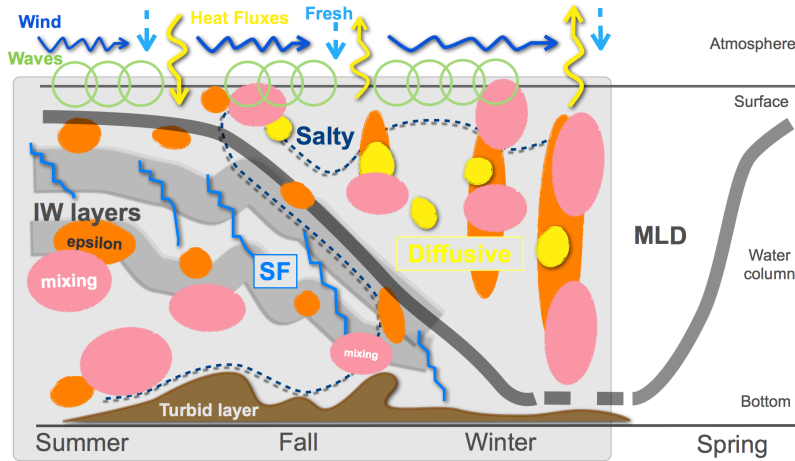

Figure 11: Schematic representation of the relevant processes identified in this study for seasonal de-stratification cycle, at the LTER-MC site in the Gulf Of Naples, by 75m deep, from July 2015 to February 2016. Freshwater (light blue dashed arrows), wind stress (royal blue arrows), buoyancy fluxes (yellow arrows), and waves (green circles) are represented at the surface. The salty tongue observed in the hydrology is depicted in dashed dark blue, while the turbid bottom layer is shown in brown. The MLD is schematized in thick gray. The two regions occupied by the first two baroclinic modes of internal waves (IW) are indicated by the shaded layers below the MLD. Schematic patches showing intensified turbulent kinetic energy dissipation and diffusion rates (mixing) are plotted in orange and pink, respectively. Salt fingering (SF) and diffusive convection regimes are schematized by the blue stairs and the yellow circles, respectively.

Appendix A Low frequency signals in the microstructure shears data

This section is motivated by the repeated observation of a low-frequency signal in our microstructure shear data, while the instrument's fall speed remained constant. This signal was observed within stratified layers, at the MLD and below the MLD, depicting vertical patterns during our survey (**Fig. A1**). We propose here a first attempt to separate parts of the signal that may be due to strong thermal gradients (pyro-effect, as discussed after), and other ones possibly due to other noise sources, or real energetic motions. The shear probes are sensitive to velocity fluctuations at frequencies greater than 0.1 Hz, but the signals are often high-pass filtered at higher frequencies ($\sim$0.4 Hz) before computing the spectra and the dissipation rate. Here we intended to carefully use the low frequency part of shear signals since no other sources of velocity shear were available. However, it is most likely that the low-frequency response in the micro-structure shear data is due to passing through strong thermal gradients, an effect known as the pyro-electric effect, which cannot be interpreted as a physical shear signal (see below). Despite this, an analysis of the low frequency signal still shows some interesting patterns that are worth presenting.

For the analysis, we defined low-passed shear energy estimates $Sh_{LP}^{1;2}$ from shear 1 and 2, calculated by low-pass filtering the despiked shears at 0.1 Hz, as
$$Sh_{LP}^{1,2} = \langle \, (du/dz)^2 \, \rangle_{LP}^{0.1Hz}, \quad \langle \, (dv/dz)^2 \, \rangle_{LP}^{0.1Hz}.$$
In our dataset, structures linked to this low-frequency signal showed vertical scales of around 3 m. We show on **Fig. A1** time filtered quantities at 0.1 Hz, that are equivalent to a spatial filtering over these length scales. We note that spatial filtering has the advantage to avoid numerical negative values (e.g. if used to estimate a proper energy content).
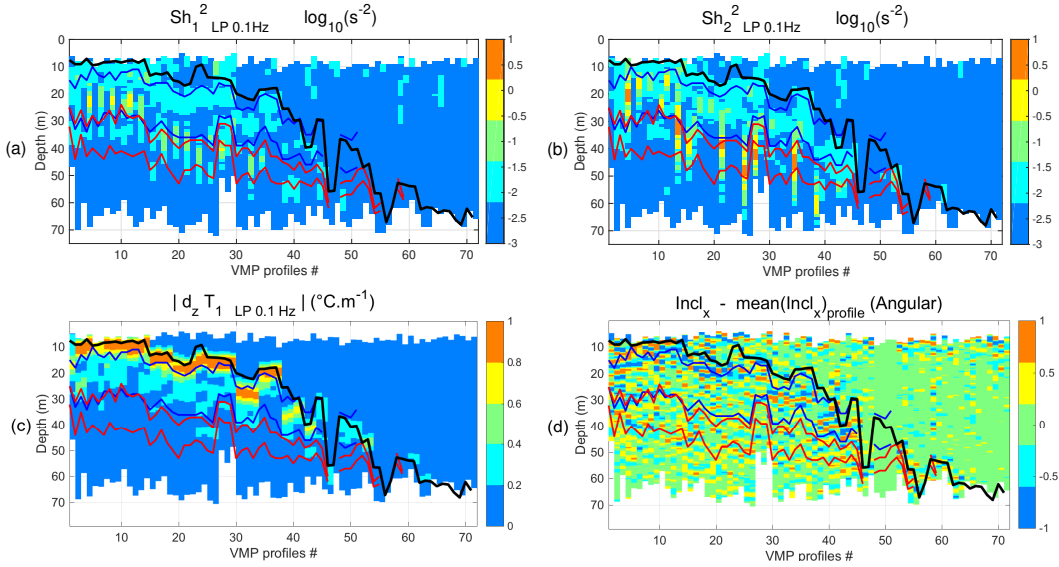

Figure A1: Square value of the microstructure shears 1 (a) and 2 (b) (i.e. du/dz and dv/dz, respectively) low pass filtered at 0.1 Hz (s^{-2}). We plotted the absolute values due to numerical negative values created by the filtering after the square operator. Profiles examples are shown on supplementary Fig. S3. (c) Microstructure gradients dT/dz ($^\circ$ m^{-1}) low-passed filtered at 0.1 Hz, and plotted in absolute value, showing subsurface layers concerned by strong vertical thermal gradients. These are mainly located between the base of the MLD and the upper limit of the envelope of the baroclinic mode B1. (d) Anomaly to the mean value of the roll inclination of the `VMP-250` (angular $^\circ$ relative to the x-axis).

Pyro-electric effect

Shear probes occasionally respond to large changes in temperature with the sudden release (or absorption) of electric charge that generates a large amplitude signal, even when no strain is applied to the ceramic beam (Lueck et al. [2002]). This effect is referred to as the pyro-electric effect (Muralt [2005]) and can occur when probes pass through large temperature gradients. To minimize this effect, the piezo-ceramic element in the shear probe is insulated from the environment by a layer of epoxy and the electronics are designed to high-pass filter the signal at 0.1 Hz (Rockland's Technical Note 005). Despite these precautions in the sensor design, some shear probes may still respond to sharp changes in temperature. In this study, the response was somewhat unpredictable and probe-dependent.

This signal was present in the subsurface shear data, when the profiler passed through the strong seasonal vertical gradients of temperature, leading to contamination of the shear signal at low frequencies between 0.1 and 1 Hz. The amplitude of the temperature gradient at the base of the MLD was approximately $1\,^\circ\mathrm{m}^{-1}$ in summer, to $0.3\,^\circ\mathrm{m}^{-1}$ during the transition from fall to winter (**Fig. A1.c**). The two shear probes responded differently when crossing the same vertical temperature gradient: shear 1 appeared to be less sensitive than shear 2 in general, with values of 3 times smaller in average, and less concerned by surface gradients. In general the resulting low-frequency signal was present up to nearly 1 Hz. To avoid temperature contamination of dissipation rate estimates in the rest of our study, we applied a high-pass filtering with a cut-off frequency of 1.5 Hz on the despiked micro-structure shears before using them to compute the spectra and estimate ϵ (see Methods). We considered the spare probe shear 2 suitable for estimating ϵ from its high-frequency content, but its low-frequency signal is probably contaminated by pyro-effect on subsurface, and intensified noisy response in the deep layers.

Low-frequency content below the strong surface gradients

As visible on (**Fig. A1**), a repetitive low frequency signal was intermittently present too in the deep layers at a 20m-distance below the MLD, both on shear 1 and 2. In contrary of the surface, these layers are concerned by moderated thermal gradients, and the shear response to this vertical structure should be presumably be free from pyro-electric contamination. We observe that this signal is distributed through the vertical envelope of the baroclinic modes of internal waves (as we defined it), and is frequently associated with small and slow oscillations of $\pm\,2°$ of the instrument roll (**Fig. A1.d**), even no specific noise contamination was visible through the accelerometers. Moreover, it appears to be co-located with other independent physical parameters, as we show it on the physical examples taken from the distinct CTD cast and the fluorometer sensor on supplementary Fig. S3. Out of affirming that we identified here a physical signal in the micro-structure shear, we decided to carry apart this low frequency shear signal through our analysis, to show its statistics, as we separated it properly from the high-passed shear used to infer ϵ. We selected only the estimation based on shear 1. To avoid numerical negative values and estimate a proper energy content, we filtered spatially instead of temporally and propose $Sh_{LP} = \langle\,(du/dz)^2\,\rangle_{LP}^{3m}$.

Possible link between Sh_{LP} and ϵ

The stratified layers possibly containing internal wave activity were remarkably co-located with the low-passed energy component Sh_{LP} events, the latter potentially being a proxy of energetic motions, even though its values are challenging to interpret. In particular, two regions exhibit enhanced low pass shear levels (**Fig. A2.a**). The first one is associated with the baroclinic mode region B1: a clear intensification is located below the MLD and follows its deepening from July to early October while another maximum is located around 20-30 m in July and early August. The second one is associated
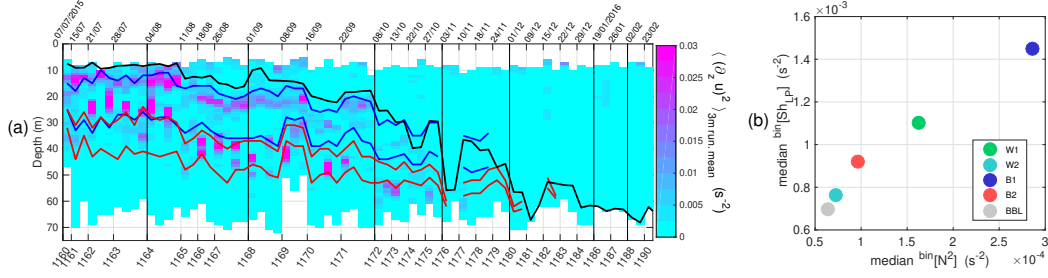
Figure A2: (a) Low pass shear energy Sh_{LP} i.e. $\langle(\partial_z u)^2\rangle_{LP}^{3m}$ (s^{-2}), $MLD_{\theta_0}^{0.4^\circ C}$ (thick black line), region of maximum energy of baroclinic mode 1 (between blue lines) and mode 2 (between red lines). The VMP profiles are plotted sequentially along the x-axis, where the MC casts references are indicated (from one to four VMP profiles by cast). Sampling dates are given on the panel top. (b) Median of Sh_{LP} (s^{-2}) in function of the median of N^2 (s^{-2}).

with B2 and it is clearly visible during August and September while having less intense imprint in July and October. Elsewhere, the low pass shear is weak whenever the stratification is weak (e.g., ML and BBL). Pdfs are shown in the supplementary information (Fig. S4). Although Sh_{LP} and ϵ are estimated over totally independent wavenumber ranges, their kurtosis-skewness relationship follows the same quadratic fit out of the log-normality (**Fig. 10.a**, dots and squares). In addition, Sh_{LP} shows a remarkable linearity as a function of the stratification intensity (**Fig. A2.b**), while ϵ does not show such a linear relationship with the stratification (**Fig. 10.a**). The Sh_{LP} estimate presented here is not conventional and its interpretation would require a thoughtful validation via a comparison with Acoustic Doppler Current Profiler (ADCP) observations. While to be considered with great caution, we documented in Fig. S5 the distribution of ϵ in function of N^2 and Sh_{LP} as proxy of the shear (Gill [1982], Monin & Yaglom [2007]). Interestingly, it shows higher ϵ values in correspondence with a weaker stratification and larger shear values. The dependence from the stratification intensity is lost in the ML (W1 and W2), while a modulation by N is suggested in the stratified layers B1, B2 and BBL, following the observations of Vladoiu et al. [2018] that tested a wave-wave parameterization for ϵ based on MacKinnon & Gregg [2003] .

Acknowledgments

References

Albanese, S., Iavazzo, P., Adamo, P., Lima, A., & De Vivo, B. (2012, 09). Assessment of the environmental conditions of the sarno river basin (south italy): A stream sediment approach. Environmental Geochemistry and Health, 35. doi: 10.1007/s10653-012-9483-x

Ardhuin, F., Marié, L., Rascle, N., Forget, P., & Roland, A. (2009, 11). Observation and estimation of lagrangian, stokes, and eulerian currents induced by wind and waves at the sea surface. Journal of Physical Oceanography, 39, 2820. doi: 10.1175/2009JPO4169.1

Baldi, M., Dalu, G., Maracchi, G., Pasqui, M., & Cesarone, F. (2006, 09). Heat waves in the mediterranean: A local feature or a larger-scale effect? International Journal of Climatology, 26, 1477–1487. doi: 10.1002/joc.1389

Barton, A., Ward, B., Williams, R., & Follows, M. (2014, 04). The impact of fine-scale turbulence on phytoplankton community structure. Limnology and Oceanography: Fluids and Environments, 4. doi: 10.1215/21573689-2651533

Belcher, S. E., Grant, A., Hanley, K., Fox-Kemper, B., Van Roekel, L., Sullivan, P., ... Polton, J. (2012, 09). A global perspective on langmuir turbulence in the ocean surface boundary layer. Geophysical Research Letters, 39, 9. doi: 10.1029/2012GL052932

Benway, H. M., Lorenzoni, L., White, A. E., Fiedler, B., Levine, N. M., Nicholson, D. P., ... Letelier, R. M. (2019). Ocean time series observations of changing marine ecosystems: An era of integration, synthesis, and societal applications. Frontiers in Marine Science, 6, 393. doi: 10.3389/fmars.2019.00393

Bouffard, D., & Boegman, L. (2013, 06). A diapycnal diffusivity model for stratified environmental flows. Dynamics of Atmospheres and Oceans, s 61–62, 14–34. doi: 10.1016/j.dynatmoce.2013.02.002

Brainerd, K. E., & Gregg, M. C. (1995). Surface mixed and mixing layer depths. Deep-Sea Research I, 42, 1521–1543.

Brody, S. R., , & Lozier, M. S. (2014). Changes in dominant mixing length scales as a driver of subpolar phytoplankton bloom initiation in the north atlantic. Geophysical Research Letter, 41 (9), 3197–3203.

Buckingham, C. E., Lucas, N. S., Belcher, S. E., Rippeth, T. P., Grant, A. L. M., , & Lesommer, J. (2019). The contribution of surface and submesoscale processes to turbulence in the open ocean surfaceboundary layer. Journal of Advances in Modeling Earth Systems, 11, 4066–4099. doi: https://doi.org/10.1029/2019MS001801

Burchard, H., & Rippeth, T. (2009, 04). Generation of bulk shear spikes in shallow stratified tidal seas. Journal of Physical Oceanography - J PHYS OCEANOGR, 39. doi: 10.1175/2008JPO4074.1

(C3S), C. C. C. S. (2017). Era5: Fifth generation of ecmwf atmospheric reanalyses of the global climate. Copernicus Climate Change Service Climate Data Store (CDS), date of access. doi: https://cds.climate.copernicus.eu/cdsapp#!/home

Carniel, S., Sclavo, M., Kantha, L., & Prandke, H. (2008, 01). Double-diffusive layers in the adriatic sea. Geophysical Research Letters, 35. doi: 10.1029/2007GL032389

Cianelli, D., D'Alelio, D., Uttieri, M., Sarno, D., Zingone, A., Zambianchi, E., & Ribera d'Alcala, M. (2017, 12). Disentangling physical and biological drivers of phytoplankton dynamics in a coastal system. Scientific Reports, 7. doi: 10.1038/s41598-017-15880-x

Cianelli, D., Falco, P., Iermano, I., Mozzillo, P., Uttieri, M., Buonocore, B., ... Zambianchi, E. (2015, 01). Inshore/offshore water exchange in the gulf of naples. Journal of Marine Systems. doi: 10.1016/j.jmarsys.2015.01.002

Cianelli, D., Uttieri, M., Buonocore, B., Falco, P., Zambardino, G., & Zambianchi, E. (2012, 08). Dynamics of a very special mediterranean coastal area: the gulf of naples. Mediterranean Ecosystems: Dynamics, Management and Conservation, 129–150.

de Boyer Montégut, C., Madec, G., Fischer, A. S., Lazar, A., & Iudicone, D. (2004, 01). Mixed layer depth over the global ocean: An examination of profile data and profile-based climatology. Journal of Geophysical Research, 109, C12003. doi: 10

.1029/2004JC002378

de Ruggiero, P., Ernesto, N., Iacono, R., Pierini, S., & Spezie, G.   (2018, 09).   A baroclinic coastal trapped wave event in the gulf of naples (tyrrhenian sea). Ocean Dynamics. doi: 10.1007/s10236-018-1221-1

Durante, S., Schroeder, K., Mazzei, L., Pierini, S., Borghini, M., & Sparnocchia, S. (2019, 01). Permanent thermohaline staircases in the tyrrhenian sea. Geophysical Research Letters. doi: 10.1029/2018GL081747

Ferrari, R., & Wunsch, C.   (2009).   Ocean circulation kinetic energy: Reservoirs, sources, and sinks. Annual Review of Fluid Mechanics, 41, 253–282.

Garrett, C., Keeley, J., & Greenberg, D.   (1978, 12).   Tidal mixing versus thermal stratification in the bay of fundy and gulf of maine.   Atmosphere-Ocean, 16, 403–423. doi: 10.1080/07055900.1978.9649046

GEBCO, C. G. (2020). Gebco 2020 grid. Retrieved from https://www.gebco.net doi: 10.5285/a29c5465-b138-234d-e053-6c86abc040b9

Gill, A. (1982, 01). Atmosphere-ocean dynamics. In (Vol. 30, p. 662).

Goodman, L., Levine, E. R., , & Lueck, R. G.   (2006).   On measuring the terms of the turbulent kinetic energy budget from an auv.   Journal of Atmospheric and Oceanic Technology, 23, 977–990.

Grant, A., & Belcher, S. E. (2009, 08). Characteristics of langmuir turbulence in the ocean mixed layer. J. Phys. Oceanogr., 39. doi: 10.1175/2009JPO4119.1

Green, M., & Coco, G. (2014, 03). Review of wave-driven sediment resuspension and transport in estuaries. Reviews of Geophysics, 52. doi: 10.1002/2013RG000437

Gregg, M. (1987, 05). Diapycnal mixing in the thermocline: A review. J. Geophys. Res., bf 92, 5249-5286. doi: 10.1029/JC092iC05p05249

Guancheng, l., Cheng, L., Zhu, J., Trenberth, K., Mann, M., & Abraham, J.   (2020, 09).   Increasing ocean stratification over the past half-century.   Nature Climate Change, 1–8. doi: 10.1038/s41558-020-00918-2

Haren, H. (2019, 07). Internal wave mixing in warming lake grevelingen. Estuarine, Coastal and Shelf Science, 226, 106298. doi: 10.1016/j.ecss.2019.106298

Haren, H., Duineveld, G., & Mienis, F.   (2019, 01).   Internal wave observations off saba bank. Frontiers in Marine Science, 5. doi: 10.3389/fmars.2018.00528

Haren, H., Piccolroaz, S., Amadori, M., Toffolon, M., & Dijkstra, H.   (2020, 11).   Moored observations of turbulent mixing events in deep lake garda, italy: Mixing events in deep lake garda.   Journal of Limnology, 80.   doi: 10.4081/jlimnol.2020.1983

Hebert, D., & de Bruyn Kops, S.   (2006, 06).   Predicting turbulence in flows with strong stable stratification. Physics of Fluids - PHYS FLUIDS, 18. doi: 10.1063/1.2204987

Hegerl, G. C., Black, E., Allan, R. P., Ingram, W. J., Polson, D., Trenberth, K. E., . . . Zhang, X. (2015). Challenges in quantifying changes in the global water cycle. Bulletin of the American Meteorological Society, 96(7), 1097–1115.

Iermano, I., Liguori, G., Iudicone, D., Buongiorno Nardelli, B., Colella, S., Zingone, A., . . . Ribera d'Alcala, M.   (2012).   Dynamics of short-living filaments and their relationship with intense rainfall events and river flows. Progress in Oceanography, 106, 118–137. doi: 10.1016/j.pocean.2012.08.003

Inoue, R., Yamazaki, H., Wolk, F., Kono, T., & Yoshida, J.   (2007, 03).   An estimation of buoyancy flux for a mixture of turbulence and double diffusion.   Journal of Physical Oceanography, 37. doi: 10.1175/JPO2996.1

Ivey, G., Winters, K., & Koseff, J. (2008, 01). Density stratification, turbulence, but how much mixing? Annual Review of Fluid Mechanics, 40, 169-184. doi: 10.1146/annurev.fluid.39.050905.110314

Johnston, T., & Rudnick, D.   (2009, 03).   Observations of the transition layer. Journal of Physical Oceanography, 39. doi: 10.1175/2008JPO3824.1

Kelly, S.   (2019, 09).   Coastally generated near-inertial waves.   Journal of Physical

Oceanography, 49. doi: 10.1175/JPO-D-18-0148.1

Kiørboe, T., & Mackenzie, B.   (1995, 12).   Turbulence-enhanced prey encounter rates in larval fish: Effects of spatial scale, larval behaviour and size.   Journal of Plankton Research, 17, 2319–2331. doi: 10.1093/plankt/17.12.2319

Koseki, S., Mooney, P., Cabos Narvaez, W. D., Gaertner, m., de la Vara, A., & Aleman, J.   (2020, 07).   Modelling a tropical-like cyclone in the mediterranean sea under present and warmer climate.
doi: 10.5194/nhess-2020-187

Large, W., & Pond, S.   (1981, 01).   Open ocean momentum flux measurement in moderate to strong winds. Journal of Physical Oceanography, 11, 336–342.

Leibovich, S.   (1983, 01).   The form and dynamics of langmuir circulations.   Annual Review of Fluid Mechanics, 15, 391-427.   doi: 10.1146/annurev.fl.15.010183 .002135

Lenn, Y.-D., Wiles, P., Torres-Valdés, S., Abrahamsen, E., Rippeth, T., Simpson, J., . . . Kirillov, S.   (2009, 03).   Vertical mixing at intermediate depths in the arctic boundary current.   Geophysical Research Letters, 36, L05601.   doi: 10.1029/2008GL036792

Li, Q., & Fox-Kemper, B.   (2017, 10).   Assessing the effects of langmuir turbulence on the entrainment buoyancy flux in the ocean surface boundary layer.   Journal of Physical Oceanography, 47. doi: 10.1175/JPO-D-17-0085.1

Li, S., Li, M., Gerbi, G., & Song, J.-B.   (2013, 10).   Roles of breaking waves and langmuir circulation in the surface boundary layer of a coastal ocean.   Journal of Geophysical Research (Oceans), 118, 5173-5187. doi: 10.1002/jgrc.20387

Lincoln, B., Rippeth, T., & Simpson, J.   (2016, 07).   Surface mixed layer deepening through wind shear alignment in a seasonally stratified shallow sea. Journal of Geophysical Research: Oceans. doi: 10.1002/2015JC011382

Linden, P.   (1976, 10).   The formation and destruction of fine-structure by double-diffusive processes. Deep Sea Research and Oceanographic Abstracts, 23, 895–908. doi: 10.1016/0011-7471(76)90820-2

Lozovatsky, I., Figueroa, M., Roget, E., Fernando, H., & Shapovalov, S.   (2005, 05). Observations and scaling of the upper mixed layer in the north atlantic. Journal of Geophysical Research, 110. doi: 10.1029/2004JC002708

Lozovatsky, I., H.J.S., F., J., P.-M., Liu, Z., Lee, J. H., & Jinadasa, S.   (2017, 08). Probability distribution of turbulent kinetic energy dissipation rate in ocean: Observations and approximations.   Journal of Geophysical Research, 122.   doi: 10.1002/2017jc013076

Lucas, N., Grant, A., Rippeth, T., Polton, J., Palmer, M., Brannigan, L., & Belcher, S. E.   (2019, 10).   Evolution of oceanic near surface stratification in response to an autumn storm.   Journal of Physical Oceanography, 49.   doi: 10.1175/JPO-D-19-0007.1

Lueck, R. (2016). Rsi technical note 028 : Calculating the rate of dissipation of turbulent kinetic energy. Rockland Scientific International Inc..

Lueck, R., Wolk, F., & Yamazaki, H.   (2002, 02).   Oceanic velocity microstructure measurements in the 20th century.   Journal of Physical Oceanography, 58, 153–174. doi: 10.1023/A:1015837020019

López-Tarazón, J., Batalla, R. J., Vericat, D., & Balasch, J.   (2010, 07).   Rainfall, runoff and sediment transport relations in a mesoscale mountainous catchment: The river isábena (ebro basin).   Catena, 82, 23-34.   doi: 10.1016/ j.catena.2010.04.005

MacKinnon, J., & Gregg, M.   (2003, 07).   Mixing on the late-summer new england shelf—solibores, shear, and stratification.   Journal of Physical Oceanography, 33, 1476–1492. doi: 10.1175/1520-0485(2003)033⟨1476:MOTLNE⟩2.0.CO;2

Mackinnon, J. A., & Gregg, M. C.   (2005).   Near-inertial waves on the new england shelf: The role of evolving stratification, turbulent dissipation, and bottom drag.

Journal of Physical Oceanography, 35, 2408–2424.

Mann, K. H., & Lazier, J. R. N. (1996). Dynamics of marine ecosystems.

Masunaga, E., Homma, H., Yamazaki, H., Fringer, O., Nagai, T., Kitade, Y., & Okayasu, A. (2015, 11). Mixing and sediment resuspension associated with internal bores in a shallow bay. Continental Shelf Research, 110. doi: 10.1016/j.csr.2015.09.022

Maurer, B., & Linden, P. (2014, 08). Intrusion-generated waves in a linearly stratified fluid. Journal of Fluid Mechanics, 752, 282–295. doi: 10.1017/jfm.2014.316

McDougall, T., & Barker, P. (2011). Getting started with teos-10 and the gibbs seawater (gsw) oceanographic toolbox. SCOR/IAPSO WG, 127, 1—28.

Moeng, & Sullivan, P. (1994, 04). A comparison of shear- and buoyancy-driven planetary boundary layer flows. J. Atm. Sci, 51, 999-1022. doi: 10.1175/1520-0469(1994)051⟨0999:ACOSAB⟩2.0.CO;2

Monin, A., & Yaglom, A. (2007). Statistical fluid mechanics, volume 1: Mechanics of turbulence.

Muralt, P. (2005). Pyroelectricity. In F. Bassani, G. L. Liedl, & P. Wyder (Eds.), Encyclopedia of condensed matter physics (pp. 441–448). Oxford: Elsevier. doi: 10.1016/B0-12-369401-9/00434-4

Nakano, H., Shimada, K., Nemoto, M., & Yoshida, J. (2014, 12). Parameterization of the eddy diffusivity due to double diffusive convection. Mer, 52, 91-98.

Nakano, H., & Yoshida, J. (2019, 05). A note on estimating eddy diffusivity for oceanic double-diffusive convection. Journal of Oceanography. doi: 10.1007/s10872-019-00514-9

Nuttall, A. H. (1971). Spectral estimation by means of overlapped fast fourier transform processing of windowed data. NUSC Tech. Rep. No. 4169. doi: https://apps.dtic.mil/sti/pdfs/AD0739315.pdf

Obukhov, A. (n.d.). Turbulentnost'v temperaturnojneodnorodnoj atmosfere ("turbulence in an atmosphere with a non-uniform temperature"). Tr. Inst. Teor. Geofiz. Akad. Nauk. SSSR., 1, 95—115.

Obukhov, A. (1971, 01). Turbulence in an atmosphere with non-uniform temperature. Boundary-Layer Meteorology, 2, 7–29. doi: 10.1007/BF00718085

Onken, R., & Brambilla, E. (1029, 01). Double diffusion in the mediterranean sea: Observation and parameterization of salt finger convection. J. Geophys. Res, 108. doi: 10.1029/2002JC001349

Osborn, T. (1980, 01). Estimates of the local rate of vertical diffusion from dissipation measurements. J. Phys. Oceanogr., 10, 83-89. doi: 10.1175/1520-0485(1980)010⟨0083:EOTLRO⟩2.0.CO;2

Osborn, T. (1998, 01). Finestructure, microstructure, and thin layers. Oceanography, 11. doi: 10.5670/oceanog.1998.13

O'Brien, M., Melling, H., Pedersen, T., & MacDonald, R. (2011, 08). The role of eddies and energetic ocean phenomena in the transport of sediment from shelf to basin in the arctic. Journal of Geophysical Research (Oceans), 116, 8001-. doi: 10.1029/2010JC006890

Passaro, S., Tamburrino, S., Vallefuoco, M., Gherardi, S., Sacchi, M., & Guido, V. (2016, 06). High-resolution morpho-bathymetry of the gulf of naples, eastern tyrrhenian sea. Journal of Maps, 1–8. doi: 10.1080/17445647.2016.1191385

Pastor, F., Valiente, J. A., , & Palau, J. L. (2018). Sea surface temperature in the mediterranean: Trends and spatial patterns (1982–2016). Pure and Applied Geophysics, 175, 4017—4029. doi: https://doi.org/10.1007/s00024-017-1739-z

Pearson, B., & Fox-Kemper, B. (2018, 02). Log-normal turbulence dissipation in global ocean models. Physical Review Letters, 120. doi: 10.1103/PhysRevLett.120.094501

Pingree, R., Holligan, P., Mardell, G., & Head, R. (1976, 11). The influence of physical stability on spring, summer and autumn phytoplankton blooms in the

celtic sea. Journal of the Marine Biological Association of the United Kingdom, 56, 845–873. doi: 10.1017/S0025315400020919

Pinkel, R., Goldin, M., Smith, J., Sun, O., Aja, A., Bui, M., & Hughen, T. (2011, 03). The wirewalker: A vertically profiling instrument carrier powered by ocean waves. Journal of Atmospheric and Oceanic Technology, 28, 426–435. doi: 10.1175/2010JTECHO805.1

Pisano, A., Marullo, S., Artale, V., Falcini, F., Yang, C., Leonelli, F., . . . Buongiorno Nardelli, B. (2020, 01). New evidence of mediterranean climate change and variability from sea surface temperature observations. Remote Sensing, 12. doi: 10.3390/rs12010132

Polton, J., Smith, J., Mackinnon, J., & Tejada-Martínez, A. (2008, 07). Rapid generation of high-frequency internal waves beneath a wind and wave forced oceanic surface mixed layer. Geophysical Research Letters, 35. doi: 10.1029/2008GL033856

Prairie, J., Sutherland, K., Nickols, K., & Kaltenberg, A. (2012, 04). Biophysical interactions in the plankton: A cross-scale review. Limnology and Oceanography: Fluids and Environments, 2. doi: 10.1215/21573689-1964713

Ribera d'Alcala, M., Conversano, F., Corato, F., Licandro, P., Mangoni, O., Marino, D., . . . Zingone, A. (2004, 04). Seasonal patterns in plankton communities in pluriannual time series at a coastal mediterranean site (gulf of naples): An attempt to discern recurrences and trends. Scientia Marina, 68, 65–83.

Roemmich, D., Alford, M., Claustre, H., Johnson, K., King, B., Moum, J., . . . Yasuda, I. (2019, 08). On the future of argo: A global, full-depth, multi-disciplinary array. Frontiers in Marine Science, 6. doi: 10.3389/fmars.2019.00439

Ruddick, B. (1983, 10). A practical indicator of the stability of the water column to double-diffusive activity. Deep Sea Research Part A. Oceanographic Research Papers, 30, 1105–1107. doi: 10.1016/0198-0149(83)90063-8

Ruddick, B., Anis, A., & Thompson, K. (2000, 11). Maximum likelihood spectral fitting: The batchelor spectrum. Journal of Atmospheric and Oceanic Technology, 17, 1541–1555. doi: 10.1175/1520-0426(2000)017⟨1541:MLSFTB⟩2.0.CO;2

Ruddick, B., & Richards, K. (2003, 03). Oceanic thermohaline intrusions: Observations. Progress In Oceanography, 56, 499–527. doi: 10.1016/S0079-6611(03)00028-4

Ruddick, B., & Turner, J. (1979, 08). The vertical length scale of double-diffusive intrusions. Deep Sea Research Part A. Oceanographic Research Papers, 26, 903–913. doi: 10.1016/0198-0149(79)90104-3

Sayol, J., Orfila, A., & Oey, L.-Y. (2016, 05). Wind induced energy-momentum distribution along the ekman-stokes layer. application to the western mediterranean sea climate. Deep Sea Research Part I Oceanographic Research Papers, 111, 34-49. doi: 10.1016/j.dsr.2016.01.004

Schopflocher, T., & Sullivan, P. (2005, 06). The relationship between skewness and kurtosis of a diffusing scalar. Boundary-Layer Meteorology, 115, 341–358. doi: 10.1007/s10546-004-5642-7

Schultze, L., Merckelbach, L., & Carpenter, J. (2017, 10). Turbulence and mixing in a shallow shelf sea from underwater gliders. Journal of Geophysical Research: Oceans. doi: 10.1002/2017jc012872

Shang, X., Qi, Y., Chen, G., Liang, C., Lueck, R., Prairie, B., & Li, H. (2016, 10). An expendable microstructure profiler for deep ocean measurements. Journal of Atmospheric and Oceanic Technology, 34. doi: 10.1175/JTECH-D-16-0083.1

Shih, L., Koseff, J., & Ivey, G. (2005, 02). Parameterisation of turbulent fluxes and scales using homogeneous sheard stratified turbulence simulations. Journal of Fluid Mechanics, 525, 193 - 214. doi: 10.1017/S0022112004002587

Skliris, N., Marsh, R., Josey, S. A., Good, S. A., Liu, C., & Allan, R. P. (2014). Salinity changes in the world ocean since 1950 in relation to changing sur-

face freshwater fluxes. Climate Dynamics, 43(3-4), 709–736. doi: 10.1007/s00382-014-2131-7

Somavilla, R., Gonzalez-Pola, C., , & Fernandez-Diaz, J. (2017). The warmer the ocean surface, the shallower the mixed layer. how much of this is true? Journal of Geophysical Research, 122(9), 7698–7716. doi: 10.1002/2017JC013125

Sullivan, P., & McWilliams, J. (2019, 11). Langmuir turbulence and filament frontogenesis in the oceanic surface boundary layer. Journal of Fluid Mechanics, 879, 512-553. doi: 10.1017/jfm.2019.655

Sutherland, G., Christensen, K., & Ward, B. (2014, 03). Evaluating langmuir turbulence in the oceanic boundary layer. Journal of Geophysical Research: Oceans, 119, n/a-n/a. doi: 10.1002/2013JC009537

Sverdrup, H. (1953, 01). On conditions for the vernal blooming of phytoplankton. J. Cons. int. Explor. Mer, 18, 287–295. doi: 10.1093/icesjms/18.3.287

Thorpe, S. (2004, 01). Langmuir circulation. Annu. Rev. Fluid Mech, 36, 55-79. doi: 10.1146/annurev.fluid.36.052203.071431

Thorpe, S. A. (2005). The turbulent ocean. Cambridge University Press.

Turner, J. (1967, 10). Salt fingers across a density interface. Deep Sea Research and Oceanographic Abstracts, 14, 599-611. doi: 10.1016/0011-7471(67)90066-6

Turner, J. (1973, 01). Buoyancy effects in fluids. doi: 10.1017/CBO9780511608827

Turner, J. (1983). Oceanic fine and microstructure. Brewer P.G. (eds) Oceanography.

Verspecht, F., Rippeth, T., Howarth, M., Souza, A., Simpson, J., & Burchard, H. (2009, 11). Processes impacting on stratification in a region of freshwater influence: Application to liverpool bay. Journal of Geophysical Research, 114. doi: 10.1029/2009JC005475

Vladoiu, A., Bouruet-Aubertot, P., Cuypers, Y., Ferron, B., Schroeder, K., Borghini, M., . . . Ben Ismail, S. (2018, 05). Turbulence in the sicily channel from microstructure measurements. Deep Sea Research Part I: Oceanographic Research Papers. doi: 10.1016/j.dsr.2018.05.006

Vladoiu, A., Bouruet-Aubertot, P., Cuypers, Y., Ferron, B., Schroeder, K., Borghini, M., . . . Ben Ismail, S. (2019, 05). Mixing efficiency from microstructure measurements in the sicily channel. Ocean Dynamics, 69. doi: 10.1007/s10236-019-01274-2

Volosciuk, C., Maraun, D., Semenov, V. A., Tilinina, N., Gulev, S. K., , & Latif, M. (2016). Rising mediterranean sea surface temperatures amplify extreme summer precipitation in central europe. Scientific Reports, 6(32450). doi: 10.1038/srep32450

Washburn, L., Swenson, M., Largier, J., Kosro, P., & Ramp, S. (1993, 10). Cross-shelf sediment transport by an anticyclonic eddy off northern california. Science (New York, N.Y.), 261, 1560-4. doi: 10.1126/science.261.5128.1560

Wheeler, J. D., Secchi, E., Rusconi, R., , & Stocker, R. (2019). Not just going with the flow: The effects of fluid flow on bacteria and plankton. The Annual Review of Cell and Developmental Biology.

Wihsgotta, J. U., Sharples, J., Hopkins, J. E., Woodward, E. M. S., Hulld, T., Greenwood, N., . . . Sivyer, D. B. (2019). Observations of vertical mixing in autumn and its e ect on the autumn phytoplankton bloom. Progress in Oceanography, 177.

Wolk, F., Yamazaki, H., Seuront, L., & Lueck, R. (2002, 05). A new free-fall profiler for measuring biophysical microstructure. Journal of Atmospheric and Oceanic Technology, 19. doi: 10.1175/1520-0426(2002)019⟨0780:ANFFPF⟩2.0.CO;2

Woodson, C. (2018, 01). The fate and impact of internal waves in nearshore ecosystems. Annual Review of Marine Science, 10. doi: 10.1146/annurev-marine-121916-063619

Wunsch, C., & Ferrari, R. (2004). Vertical mixing, energy, and the general circulation of the oceans. Annual Review of Fluid Mechanics, 36, 281–314.

Xie, X., & Li, M. (2019, 04). Generation of internal lee waves by lateral circulation in a coastal plain estuary. Journal of Physical Oceanography, 49. doi: 10.1175/JPO-D-18-0142.1

Zhang, H.-M., & Talley, L. (1998, 10). Heat and buoyancy budgets and mixing rates in the upper thermocline of the indian and global oceans. Journal of Physical Oceanography, 28, 1961–1978. doi: 10.1175/1520-0485(1998)028⟨1961:HABBAM⟩2.0.CO;2

Zhang, J., Schmitt, R., & Huang, R. (1998, 04). Sensitivity of the gfdl modular ocean model to parameterization of double-diffusive processes. Journal of Physical Oceanography - J PHYS OCEANOGR, 28, 589-605. doi: 10.1175/1520-0485(1998)028⟨0589:SOTGMO⟩2.0.CO;2

Zhang, W., Villarini, G., Scoccimarro, E., & Napolitano, F. (2020, 05). Examining the precipitation associated with medicanes in the high-resolution era-5 reanalysis data. International Journal of Climatology. doi: 10.1002/joc.6669

Zika, J. D., Skliris, N., Nurser, A. J. G., Josey, S. A., Mudryk, L., Laliberte, F., & Marsh, R. (2015). Maintenance and broadening of the ocean's salinity distribution by the water cycle. Journal of Climate, 28(24), 9550–9560. doi: 10.1175/JCLI-D-15-0273.1

Zingone, A., D'Alelio, D., Mazzocchi, M. G., Montresor, M., & Sarno, D. (2019, 05). Time series and beyond: Multifaceted plankton research at a marine mediterranean lter site. Nature Conservation, 34, 273–310. doi: 10.3897/natureconservation.34.30789

Supporting Information for "Microstructure observations of the summer-to-winter destratification at a coastal site in the Gulf of Naples"

Florian Kokoszka[1], Fabio Conversano[1], Daniele Iudicone[1], Bruno Ferron[2],

Pascale Bouruet-Aubertot[3], Justine Mc Millan[4]

[1]Stazione Zoologica Anton Dohrn, Naples, Italy

[2]Univ. Brest, CNRS, IFREMER, IRD, Laboratoire d'Océanographie Physique et Spatiale (LOPS), IUEM, Plouzané, France

[3]Sorbonne Université (UPMC, Univ Paris 06)-CNRS-IRD-MNHN, LOCEAN, Paris, France

[4]Rockland Scientific International Inc., Victoria, Canada

Contents of this file

Introduction We provide in Tab. S1 the list and dates of the CTD casts (referenced as MC), including the sequence of VMP profiles. Statistics of the Turners's regimes by layers

―――――

Corresponding author: F. Kokoszka, Department of Research Infrastructures for Marine Biological Resources (RIMAR), Stazione Zoologica A. Dohrn, villa Comunale, 80121, Naples, Italy (florian.kokoszka@szn.it)

July 6, 2021, 9:27pm

are given in Tab. S2. We provide in Fig. S1 some details of the VMP data processing. The stratification's decomposition through baroclinic modes of internal waves is presented in Fig. S2. Vertical profiles of some MC casts for CTD and VMP data are detailed in Fig. S3. Additional statistics of the Sh_{LP} are presented in Fig. S4 and Fig. S5.

Tab S1. Metadata We present in Tab. S1 the dates and references of CTD and VMP profiles.

Tab S2. Turner's regimes We present in Tab. S2 some statistics from the Turner's analysis.

Fig S1. VMP processing We calculated dissipation rates of turbulent kinetic energy with the ODAS Toolbox provided by Rockland (version 4.4.06). We present on Fig. S1 the quality metric of our data with the Figure of Merit (FM) and two examples of Nasmyth's fit illustrating stratified and weakly stratified water-column cases.

Fig S2. Stratification and baroclinic modes of internal waves Ocean dynamic vertical modes were calculated for each profile from N^2, using the routine from Klink (1999). Profiles were smoothed by filtering over a 10m-length running window before applying the algorithm. We focused then on the two first modes B1 and B2 that presented the largest variances. We defined then some vertical envelopes for the layers of these two modes. For each profile, we considered the layer containing the shear maxima of the first two baroclinic modes. To achieve this, we normalized the shear maxima to 1 and identified the depths interval, as the upper and lower depths of the layer where values were > 0.9. To consider only stratified part of the water-column, calculations were made below the MLD. A comparison between N^2 calculated from both VMP-microCT and CTD hydrology, with a plot of the baroclinic modes and their envelope is shown on Fig. S2.

Fig S3. VMP casts's examples We present on Fig. S3 vertical profiles from the VMP casts MC1173, MC1175 and MC1180 to show some examples of the rich structure of the water-column. Cast MC1180 illustrates a winter case when the MLD reaches the proximity of the bottom layer, where a turbid feature is present from 62 to 70m. In the stratified cases of casts MC1173 and MC1175, even more thin, turbid bottom layers are present too below 60m. Weak double salt fingering layers can be seen too, below the MLD between 25 and 45m, with Tu angles around 60° and 50°, respectively. All casts show intensified Sh_{LP} located below the passage of the local density gradients.

Fig S4. Probability density functions of the low-frequency content of the micro-structure shear The stratified layers possibly containing internal wave activity were remarkably co-located with the low-passed energy component Sh_{LP} (see Appendix) that could be an interesting proxy of energetic motions, even its values are not possible to interpret. A clear pattern is visible (see Fig. A1), with intense occurrences distributed into the highly stratified layers during the summer period, and then into the subsurface layers marking the baroclinic modes $B1$ and $B2$. Two tendencies are visible. A first one below the MLD and B1 in July and early August, and a second one through both B1 and B2 layers from mid-August to the end of October. In terms of distribution (Fig. S4), the most intense values of around 1×10^{-3} s^{-2} are contained into the bins below the MLD in the B1 bin (Fig. S4.b). Surface layers are dominated by weaker values of around 6×10^{-2} s^{-2} (Fig. S4.a).

Fig S5. Dissipation rates in function of N^2 and Sh_{LP} Even Sh_{LP} is challenging to use and interpret, a classical display averaged values of ϵ ($W.kg^{-1}$) by intervals ΔN^2 (s^{-2}) and ΔSh_{LP} (s^{-2}) is shown on Fig. S5.

July 6, 2021, 9:27pm

Table S1.   General information of the MC-CTD casts and VMP profiles.

VMP#	CTD# (MC cast)	Date	VMP#	CTD# (MC cast)	Date	VMP#	CTD# (MC cast)	Date
1	1160	07/07/2015 08:01	24	1168	01/09/2015 07:46	47	1176	03/11/2015 09:31
2	1161	15/07/2015 09:39	25	1168	01/09/2015 08:40	48	1177	10/11/2015 09:24
3	1161	15/07/2015 09:41	26	1168	01/09/2015 08:43	49	1177	10/11/2015 09:27
4	1162	21/07/2015 08:04	27	1169	08/09/2015 07:57	50	1178	18/11/2015 09:23
5	1162	21/07/2015 08:07	28	1169	08/09/2015 08:00	51	1178	18/11/2015 09:25
6	1162	21/07/2015 08:55	29	1169	10/09/2015 08:46	52	1179	24/11/2015 09:49
7	1163	28/07/2015 08:23	30	1170	16/09/2015 08:27	53	1179	24/11/2015 09:52
8	1163	28/07/2015 09:26	31	1170	16/09/2015 08:30	54	1180	01/12/2015 09:08
9	1163	28/07/2015 09:29	32	1170	16/09/2015 10:18	55	1180	01/12/2015 09:11
10	1163	28/07/2015 08:20	33	1170	16/09/2015 10:21	56	1181	09/12/2015 09:27
11	1164	04/08/2015 07:49	34	1171	22/09/2015 07:55	57	1181	09/12/2015 09:30
12	1164	04/08/2015 07:51	35	1171	22/09/2015 07:58	58	1182	15/12/2015 09:32
13	1164	04/08/2015 08:45	36	1171	22/09/2015 08:53	59	1182	15/12/2015 09:35
14	1164	04/08/2015 08:48	37	1171	22/09/2015 08:56	60	1183	22/12/2015 09:01
15	1165	11/08/2015 08:11	38	1172	08/10/2015 08:38	61	1183	22/12/2015 09:04
16	1165	11/08/2015 08:14	39	1172	08/10/2015 08:40	62	1184	29/12/2015 09:01
17	1166	18/08/2015 07:55	40	1173	13/10/2015 08:21	63	1184	29/12/2015 09:04
18	1166	18/08/2015 07:58	41	1173	13/10/2015 08:24	64	1186	19/01/2016 08:36
19	1167	26/08/2015 07:34	42	1174	22/10/2015 08:09	65	1186	19/01/2016 08:39
20	1167	26/08/2015 07:37	43	1174	22/10/2015 08:12	66	1187	26/01/2016 09:59
21	1167	26/08/2015 08:59	44	1175	27/10/2015 09:34	67	1187	26/01/2016 10:02
22	1167	26/08/2015 09:02	45	1175	27/10/2015 09:37	68	1188	02/02/2016 11:29
23	1168	01/09/2015 07:44	46	1176	03/11/2015 09:28	69	1188	02/02/2016 11:32
						70	1190	23/02/2016 10:19
						71	1190	23/02/2016 10:22

July 6, 2021, 9:27pm

Table S2.   (a) Decibar occupation of the Turner's regimes for the whole dataset. (b) Statistics

by layers and period bins for the double diffusive and (c) diffusive convection regimes.

(a) General

Regime	SF	Stable	Diffusive	Instable	All
Count	1202	2159	396	142	3899
%	30.8%	55.4%	10.2%	3.6%	100

(b) Double diffusive regime (salt fingers)

Bin	%	mean Tu mean R_ρ	median	std	SF%	Stable%	Diff.%	Inst.%	Bin count
All	100	54.7 (Tu) 8.88 (R_ρ)	51.8 6.79	9.3 6.82	30.80	55.4	10.2	3.6	3899
surface-MLD	32	60.5 6.03	58.7 3.77	11.2 5.67	24.7	41.8	25	8.5	1573
MLD-bottom	68	52.1 10.4	50.2 8.36	6.61 6.89	35	64.6	0.1	0.3	2326
W1	13	59.8 6.07	58.7 3.88	10.4 5.54	28.1	46.2	22.7	3	572
W2	19	61.0 6.01	58.4 3.69	11.8 5.77	22.8	39.3	26.3	11.7	1001
B1	39	51.5 10.5	50.3 8.57	5.34 6.59	59.9	39.3	0.4	0.4	778
B2	13	53.4 10.1	50.5 7.82	8.97 7.67	29.6	69.5	0	0.9	544
BBL	6	55.02 8.67	52.4 5.79	8.46 6.43	8.8	90.9	0.2	0	803

(c) Diffusive regime (convection)

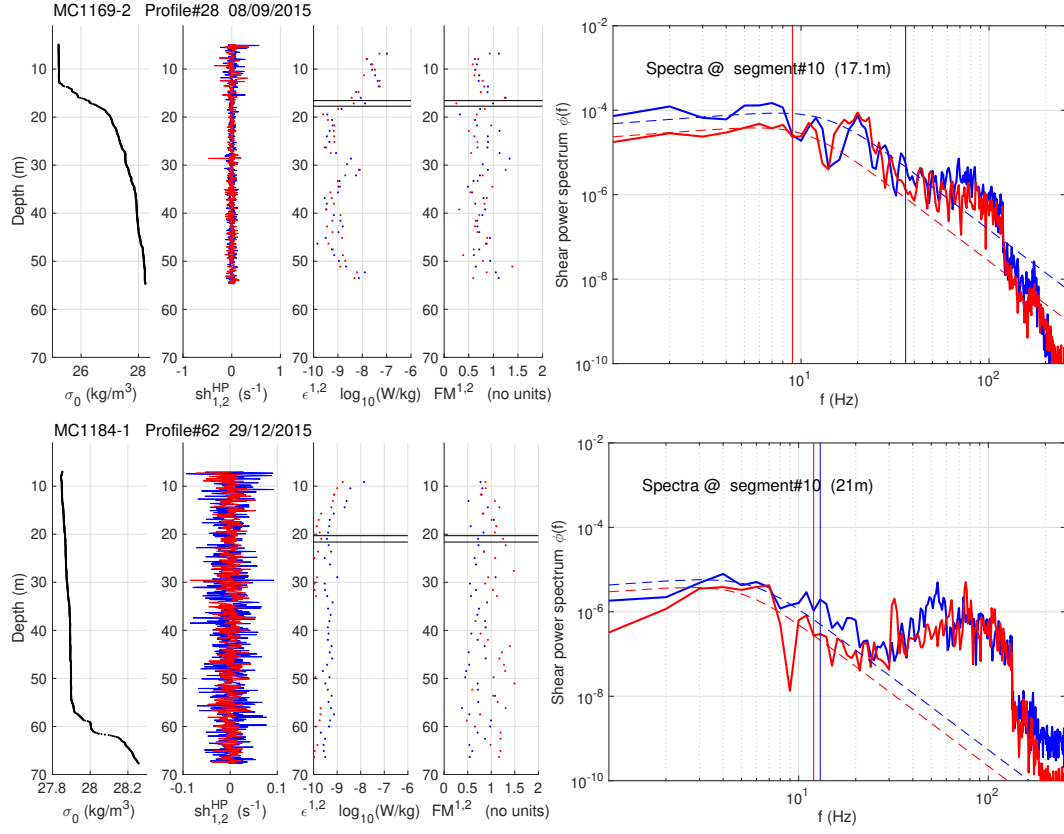| Bin	%	mean Tu mean R_ρ	median	std	SF%	Stable%	Diff.%	Inst.%	Bin count
All	100	-67.4 (Tu) 0.43 (R_ρ)	-67.9 0.42	11.9 0.25	30.8	55.4	10.	3.6	3899
surface-MLD	99	-67.57 0.43	-68.1 0.42	11.8 0.25	24.7	41.8	25	8.5	1573
MLD-bottom	1	-49.3 0.07	-49.1 0.07	3.4 0.06	35	64.6	0.1	0.3	2326
W1	33	-63.6 0.35	-63.0 0.32	10.04 0.20	28.1	46.2	22.7	3	572
W2	66	-69.50 0.48	-71.25 0.49	12.21 0.26	22.80	39.30	26.30	11.70	1001
B1	1	-66.8 0.42	-76.2 0.60	17.6 0.34	59.9	39.3	0.4	0.4	778
B2	0	NaN NaN	NaN NaN	NaN NaN	29.6	69.5	0	0.9	544
BBL	1	-47.6 0.04	-47.6 0.04	2.14 0.03	8.8	90.9	0.2	0	803

July 6, 2021, 9:27pm

Figure S1. Examples of Nasmyth's spectra fits, for stratified (top) and weakly stratified cases (bottom). The final ϵ is the mean value of the individual estimates ϵ_1 and ϵ_2, excepted for the case where only one value is available (for example after rejection if $FM > 1.5$). Finally, if two estimates differ by one order of magnitude, the lowest is kept.
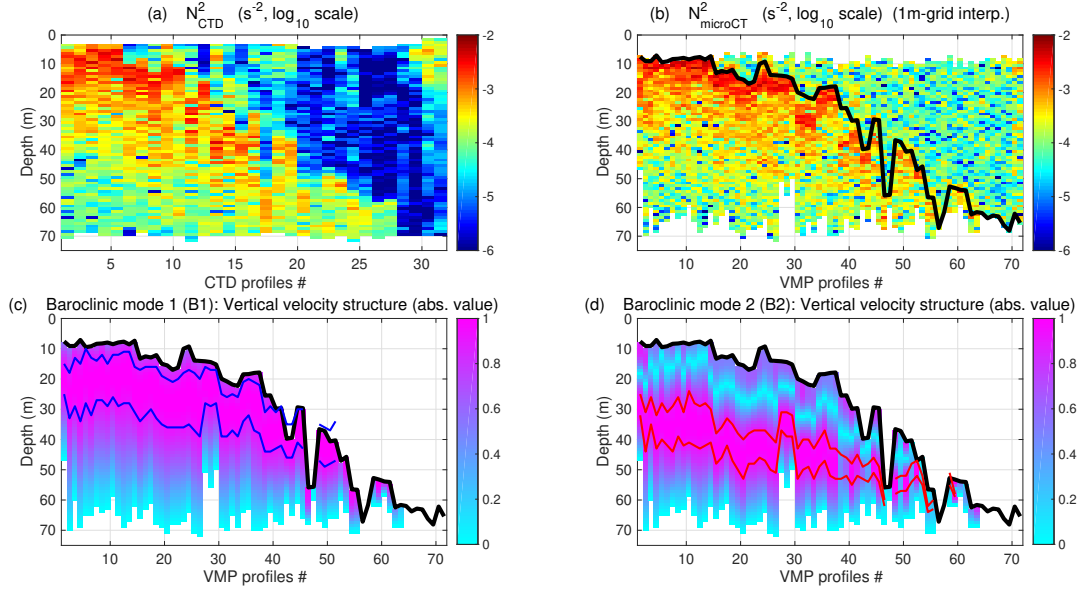
Figure S2. (a) Profiles of the Brunt-Väisälä frequency N^2_{ctd} (s^{-2}) computed from the hydrology obtained with the CTD `Seabird 911+` and (b) N^2_{vmp} (s^{-2}) computed from the hydrology obtained with the micro-CT nose-mounted on the `VMP-250`. Both quantities have been calculated with the dedicated Gibbs Seawater function. $MLD^{\theta}_{0.4°}$ is shown In thick black. (c) Vertical velocity structure (non-dimensional) of the first and (d) second baroclinic modes calculated from N^2_{vmp}. $MLD^{0.4°C}_{\theta_0}$ (thick black line), region of maximum energy of baroclinic mode 1 (between blue lines) and mode 2 (between red lines).
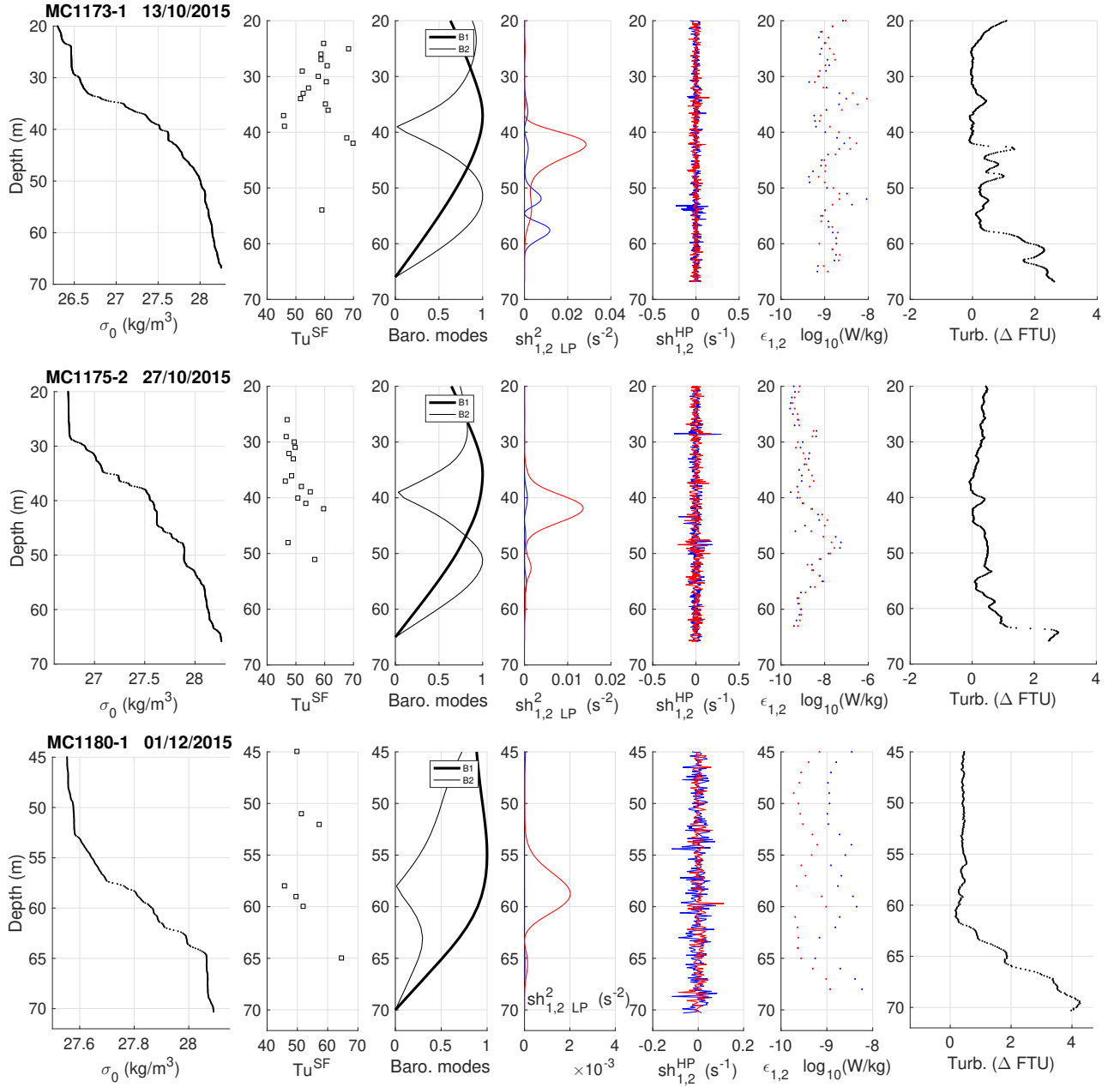
Figure S3.   Top to bottom : profiles from the VMP casts MC1173, MC1175 and MC1180. From left to right : σ_0 (kg m^{-3}), Turner angles (°) into the salt-fingering regime, first and second vertical baroclinic modes (non-dimensional), low-passed energy shears Sh_{LP} (s^{-2}), hi-passed shears (s^{-1}) used to estimate ϵ (W kg^{-1}), and turbidity (ΔFTU, offset from the reference value -2.5). For shears and ϵ, blue and red refers to the respective shear probes 1 and 2.
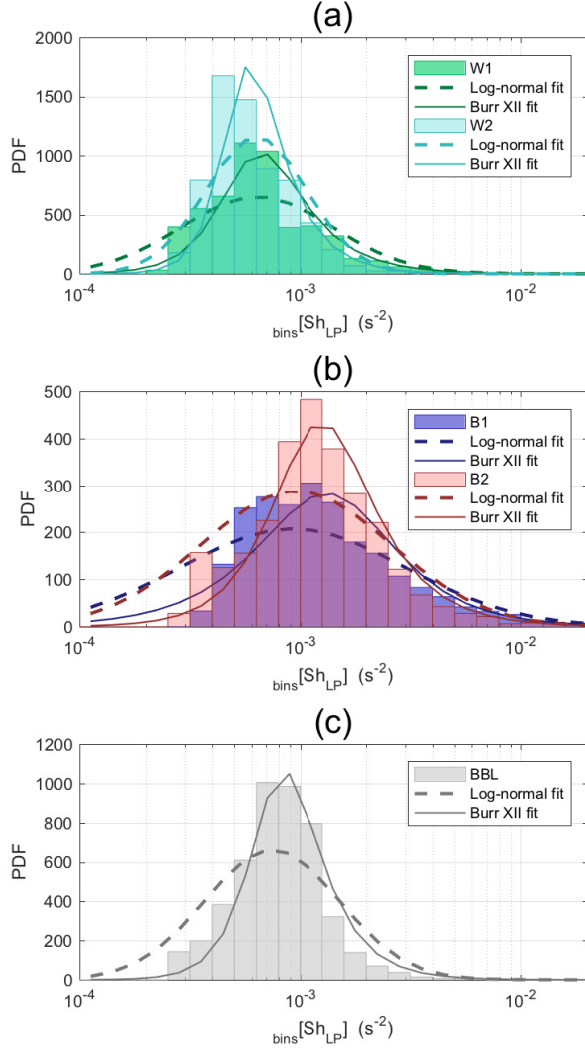
July 6, 2021, 9:27pm

Figure S4. Pdfs of Sh_{LP} i.e. $\langle (\partial_z u)^2 \rangle_{LP}^{3m}$ (s^{-2}) through (a) temporal bins W1 and W2, and (b,c) vertical bins B1, B2 and BBL. The fits of the log-normal and Burr type XII distributions are indicated with the dashed and solid lines, respectively.
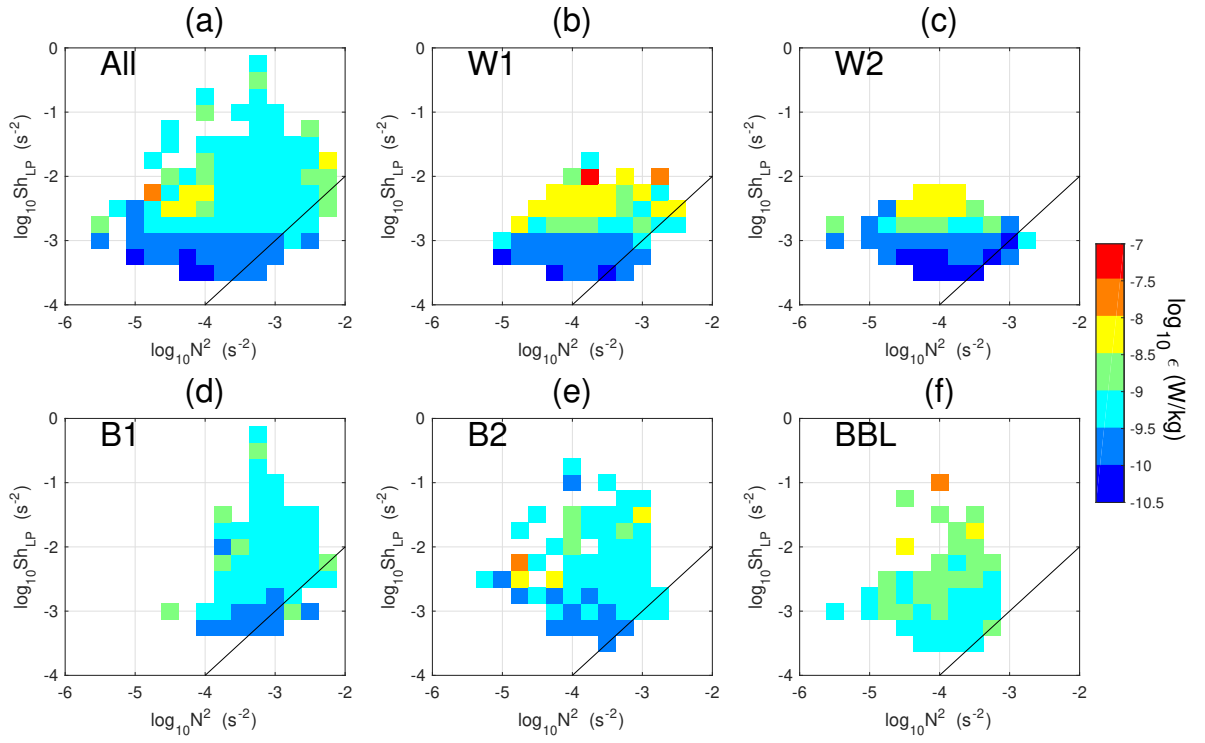
Figure S5. Averaged values of ϵ $(W.kg^{-1})$ by intervals ΔN^2 (s^{-2}) and ΔSh_{LP} (s^{-2}), for the different groups of periods and layers. Intervals ΔN^2 and ΔSh_{LP} have been defined $= 0.25$ in the logarithmic domain (log_{10}). Black line indicates $\frac{N^2}{Sh_{LP}} = 1$.